

Extended Shock Breakout and Early Circumstellar Interaction in SN 2024ggi

MANISHA SHRESTHA,¹ K. AZALEE BOSTROEM,^{1,*} DAVID J. SAND,¹ GRIFFIN HOSSEINZADEH,¹ JENNIFER E. ANDREWS,² YIZE DONG (董一泽),³ EMILY HOANG,³ DARYL JANZEN,⁴ JENIVEVE PEARSON,¹ JACOB E. JENCSON,⁵ M. J. LUNDQUIST,⁶ DARSHANA MEHTA,³ ARAVIND P. RAVI,³ NICOLÁS MEZA RETAMAL,³ STEFANO VALENTI,³ PETER J. BROWN,⁷ SAURABH W. JHA,⁸ COLIN MACRIE,⁸ BRIAN HSU,¹ JOSEPH FARAH,^{9,10} D. ANDREW HOWELL,^{9,10} CURTIS MCCULLY,⁹ MEGAN NEWSOME,^{9,10} ESTEFANIA PADILLA GONZALEZ,^{9,10} CRAIG PELLEGRINO,¹¹ GIACOMO TERRERAN,^{9,10} LINDSEY KWOK,⁸ NATHAN SMITH,¹ MICHAELA SCHWAB,⁸ AIDAN MARTAS,³ RICARDO R. MUNOZ,¹² GUSTAVO E. MEDINA,¹³ TING S. LI,¹³ PAULA DIAZ,¹² DAICHI HIRAMATSU,^{14,15} BRAD E. TUCKER,¹⁶ J. C. WHEELER,¹⁷ XIAOFENG WANG,¹⁸ QIAN ZHAI,¹⁹ JUJIA ZHANG,^{19,20} ANJASHA GANGOPADHYAY,²¹ YI YANG,¹⁸ AND CLAUDIA P. GUTIÉRREZ^{22,23}

¹Steward Observatory, University of Arizona, 933 North Cherry Avenue, Tucson, AZ 85721-0065, USA

²Gemini Observatory, 670 North A‘ohoku Place, Hilo, HI 96720-2700, USA

³Department of Physics and Astronomy, University of California, Davis, 1 Shields Avenue, Davis, CA 95616-5270, USA

⁴Department of Physics & Engineering Physics, University of Saskatchewan, 116 Science Place, Saskatoon, SK S7N 5E2, Canada

⁵IPAC, California Institute of Technology, 1200 East California Boulevard, Pasadena, CA 91125, USA

⁶W. M. Keck Observatory, 65-1120 Māmalahoa Highway, Kamuela, HI 96743-8431, USA

⁷Department of Physics and Astronomy, Texas A&M University, 4242 TAMU, College Station, TX 77843, USA

⁸Department of Physics and Astronomy, Rutgers, the State University of New Jersey, 136 Frelinghuysen Road, Piscataway, NJ 08854-8019, USA

⁹Las Cumbres Observatory, 6740 Cortona Drive, Suite 102, Goleta, CA 93117-5575, USA

¹⁰Department of Physics, University of California, Santa Barbara, CA 93106-9530, USA

¹¹Department of Astronomy, University of Virginia, Charlottesville, VA 22904, USA

¹²Departamento de Astronomía, Universidad de Chile, Camino El Observatorio 1515, Las Condes, Santiago, Chile

¹³David A. Dunlap Department of Astronomy and Astrophysics, University of Toronto, 50 St. George Street, Toronto, Ontario, M5S 3H4 Canada

¹⁴Center for Astrophysics | Harvard & Smithsonian, 60 Garden Street, Cambridge, MA 02138-1516, USA

¹⁵The NSF AI Institute for Artificial Intelligence and Fundamental Interactions

¹⁶Mt. Stromlo Observatory, The Research School of Astronomy and Astrophysics, Australian National University, ACT 2601, Australia

¹⁷University of Texas at Austin, 1 University Station C1400, Austin, TX 78712-0259, USA

¹⁸Physics Department and Tsinghua Center for Astrophysics, Tsinghua University, Beijing, 100084, People’s Republic of China

¹⁹Yunnan Observatories (YNAO), Chinese Academy of Sciences (CAS), Kunming, 650216, People’s Republic of China

²⁰International Centre of Supernovae, Yunnan Key Laboratory, Kunming 650216, People’s Republic of China

²¹Oskar Klein Centre, Department of Astronomy, Stockholm University, Albanova University Centre, SE-106 91 Stockholm, Sweden

²²Institut d’Estudis Espacials de Catalunya (IEEC), Edifici RDIT, Campus UPC, 08860 Castelldefels (Barcelona), Spain

²³Institute of Space Sciences (ICE, CSIC), Campus UAB, Carrer de Can Magrans, s/n, E-08193 Barcelona, Spain

ABSTRACT

We present high-cadence photometric and spectroscopic observations of supernova (SN) 2024ggi, a Type II SN with flash spectroscopy features, which exploded in the nearby galaxy NGC 3621 at ~ 7 Mpc. The light-curve evolution over the first 30 hours can be fit by two power law indices with a break after 22 hours, rising from $M_V \approx -12.95$ mag at +0.66 days to $M_V \approx -17.91$ mag after 7 days. In addition, the densely sampled color curve shows a strong bluerward evolution over the first few days and then behaves as a normal SN II with a redward evolution as the ejecta cool. Such deviations could be due to interaction with circumstellar material (CSM). Early high- and low-resolution spectra clearly show high-ionization flash features from the first spectrum to +3.42 days after the explosion. From the high-resolution spectra, we calculate the CSM velocity to be 37 ± 4 km s⁻¹. We also see the line strength evolve rapidly from 1.22 to 1.49 days in the earliest high-resolution spectra. Comparison of the low-resolution spectra with CMFGEN models suggests that the pre-explosion mass-loss rate of SN 2024ggi

falls in a range of 10^{-3} to $10^{-2} M_{\odot} \text{ yr}^{-1}$, which is similar to that derived for SN 2023ixf. However, the rapid temporal evolution of the narrow lines in the spectra of SN 2024ggi ($R_{\text{CSM}} \sim 2.7 \times 10^{14} \text{ cm}$) could indicate a smaller spatial extent of the CSM than in SN 2023ixf ($R_{\text{CSM}} \sim 5.4 \times 10^{14} \text{ cm}$) which in turn implies lower total CSM mass for SN 2024ggi.

Keywords: Core-collapse supernovae (304), Type II supernovae (1731), Red supergiant stars (1375), Stellar mass loss (1613), Circumstellar matter (241)

1. INTRODUCTION

Nearby core-collapse supernovae (SNe) offer an unparalleled opportunity to learn about their progenitor star systems, pre-explosion environments, and the explosions themselves. The proliferation of high-cadence time-domain surveys tied to rapid-response facilities has yielded exquisite data sets, leading to sizeable advances and new questions, many of them centered around the circumstellar material (CSM) associated with the star at explosion and the effects this material may have on the early light curves and spectra.

While it is well established that red supergiant (RSG) stars are the progenitors of normal Type II SNe (SNe II) (Smartt 2009, 2015, and references therein), the final stages of RSG evolution are still uncertain. Shock breakout (SBO) is expected when the optical depth drops below $\sim c/v_{sh}$ where c is the speed of light and v_{sh} is the shock velocity (Waxman & Katz 2017). This breakout produces flashes of X-ray/UV on short timescales (seconds to hours) and UV/optical emission on \sim day timescales from the expanding cooling envelope. The SBO duration could be attributed to light-travel time across the stellar surface which can provide a constraint on the stellar radius (Goldberg et al. 2022; Waxman & Katz 2017). However, in the presence of dense CSM these time scales can increase to days (e.g. Chugai et al. 2004; Smith & McCray 2007; Ofek et al. 2010; Dessart et al. 2017a; Haynie & Piro 2021). This SBO from dense CSM can produce ionized narrow emission lines in their spectra during this time.

A significant fraction of SNe II display narrow flash features in the days after explosion (e.g., Gal-Yam et al. 2014; Smith et al. 2015; Khazov et al. 2016; Yaron et al. 2017; Hosseinzadeh et al. 2018; Zhang et al. 2020; Tartaglia et al. 2021; Terreran et al. 2022; Bostroem et al. 2023; Jacobson-Galán et al. 2023; Bruch et al. 2023; Andrews et al. 2024), which signify interaction with the material from pre-supernova mass loss of the progenitor star. Interestingly, this material seems to be confined ($\lesssim 10^{15} \text{ cm}$) and the estimated mass-loss

rates from these early SN observations indicate $\dot{M} = 10^{-3} - 10^{-2} M_{\odot} \text{ yr}^{-1}$ (Jacobson-Galán et al. 2024a, for a recent compilation), orders of magnitude higher than values inferred for quiescent mass loss in RSGs (e.g. de Jager et al. 1988; Ekström et al. 2012; Beasor et al. 2020). Such high mass loss in the final years before explosion can also affect the early light-curve evolution, causing it to deviate from standard shock-breakout scenarios (e.g. see recent results on SN 2023ixf; Hosseinzadeh et al. 2023; Hiramatsu et al. 2023a; Li et al. 2024; Zimmerman et al. 2024).

Here, we present a new study of a very nearby core-collapse SN that showed prominent signs of interaction with dense CSM. SN 2024ggi was discovered by the Asteroid Terrestrial-Impact Last Alert System (ATLAS Tonry 2011; Tonry et al. 2018; Smith et al. 2020; Srivastav et al. 2024; Chen et al. 2024) on 2024-04-11 03:22:36 UT (MJD 60411.14; Tonry et al. 2024) in NGC 3621 (see Figure 1). It was classified as a SN II with prominent flash features on 2024-04-11 14:35:47 UT (MJD 60411.61; Zhai et al. 2024a). A tight non-detection limit was obtained by the Gravitational-wave Optical Transient Observer (GOTO; Steeghs et al. 2022) on 2024-04-10 10:56:25 UT (MJD 60410.46), with a limiting magnitude of $L = 19.5 \text{ mag}$ (Killestein et al. 2024a), less than one day before the first ATLAS detection. We use the midpoint of the last non-detection (MJD 60410.46), and first detection (MJD 60411.14) as our explosion epoch throughout this work (i.e., MJD 60410.80 ± 0.34) and all the phases in this paper are calculated based on this value. We also adopt the Cepheid-based distance to NGC3621 of $D = 7.24 \pm 0.20 \text{ Mpc}$ (Saha et al. 2006), identical to that used in Jacobson-Galán et al. (2024b). Several basic parameters associated with SN 2024ggi are shown in Table 1.

A few other studies have presented results on SN 2024ggi. In Jacobson-Galán et al. (2024b), the early light curve and low-dispersion flash spectroscopy were presented and placed in context with the larger population of CSM-interacting SNe II. Two high-resolution spectra taken the night after discovery were presented in Pessi et al. (2024), showing evolution in the flash features on ~ 7 hour time scales. An early multi-band

* LSSTC Catalyst Fellow

light curve was presented in [Chen et al. \(2024\)](#), while an analysis of the progenitor RSG was presented in [Xiang et al. \(2024\)](#). Analysis of the archival Hubble Space Telescope (HST) and *Spitzer* Space Telescope images obtained over 20 years before the SN exploded indicates that the progenitor of SN 2024ggi is consistent with a red supergiant (RSG) star with a temperature of $T = 3290^{+19}_{-27}$ K, radius of $R = 887^{+60}_{-51} R_{\odot}$, and initial mass of $M = 13 \pm 1 M_{\odot}$ ([Xiang et al. 2024](#)). [Zhang et al. \(2024a\)](#) presented high cadence early time spectra with flash features. From their analysis of these spectra they find the CSM extends to 4×10^{14} cm with a mass loss rate of $5 \times 10^{-3} M_{\odot} \text{yr}^{-1}$ and velocity of unshocked CSM to be between 20 and 40 km s⁻¹. [Soker \(2024\)](#) compared the observational data and theoretical work on SN 2024ggi with various explosion mechanisms and found that the jittering jets explosion mechanism is favored for this SN explosion.

This paper presents an extremely high-cadence early light curve and spectroscopic time sequence of SN 2024ggi, including a series of high-resolution spectra (Section 2). After estimating the line-of-sight extinction based on the measurements of the pseudo-equivalent width of the NaID lines (Section 3), we derive and interpret the intrinsic photometric and color evolution of SN 2024ggi in Section 4, including a search for precursor outbursts, the remarkable evolution seen on the first day, and a shock-cooling analysis. We analyze the spectroscopic sequence of SN 2024ggi in Section 5, with an emphasis on the flash features, their evolution, and the implications for the CSM surrounding the progenitor at the time of explosion. In Section 6, we compare SN 2024ggi with the recent SN II in M101, SN 2023ixf, which also displayed well-observed flash features, is located at nearly the same distance, and has a similar-quality data set. We summarize and conclude the results in Section 7.

2. OBSERVATIONS & DATA REDUCTION

Immediately after the discovery of SN 2024ggi, we began an intensive, high-cadence photometric and spectroscopic campaign, as described in the following sections.

2.1. Photometry

In the early hours after the discovery announcement, we acquired a nearly continuous multiband photometric sequence with the Distance Less Than 40 Mpc (DLT40; [Tartaglia et al. 2018](#)) survey’s two southern telescopes – the PROMPT5 0.4 m telescope at the Cerro Tololo International Observatory and the PROMPT-MO 0.4 m telescope at the Meckering Observatory in Australia, operated by the Skynet telescope network ([Reichart et al.](#)

Table 1. Properties of SN 2024ggi

Parameter	Value
R.A. (J2000)	11:18:22.09
Dec. (J2000)	−32:50:15.3
Last Nondetection (MJD)	60410.46
First Detection (MJD)	60411.14
Explosion Epoch (MJD) ^a	60410.80
Redshift (z) ^b	0.00221
Distance ^c	7.24 ± 0.2 Mpc
Distance modulus (μ) ^c	29.30 mag
$E(B - V)_{\text{MW}}$ ^a	0.054 ± 0.020 mag
$E(B - V)_{\text{cloud}}$ ^a	0.066 ± 0.020 mag
$E(B - V)_{\text{host}}$ ^a	0.034 ± 0.020 mag
$E(B - V)_{\text{tot}}$ ^a	0.154 ± 0.035 mag
Peak Magnitude (V_{max})	−17.72 mag
Time of V_{max} (MJD)	60417.82
Rise time (V)	7 days

^amid point of last nondetection and first detection

^bfrom the Na I D lines of the host galaxy

^cfrom [Saha et al. \(2006\)](#)

2005). Data were taken in B , V , g , r , and i , as well as a wide-band configuration. In this wide mode, the PROMPT5 telescope observations are filterless (‘Open’) and the PROMPT-MO telescope utilizes a broadband ‘Clear’ filter, both of which are calibrated to the Sloan Digital Sky Survey r band (see [Tartaglia et al. 2018](#), for further reduction details). Aperture photometry on the DLT40 multiband B , V , g , r , and i images was performed using Photutils ([Bradley et al. 2022](#)) and was then calibrated to the American Association of Variable Star Observers (AAVSO) Photometric All-Sky Survey (APASS; [Henden et al. 2009](#)).

Further high-cadence multiband observations were taken with the Las Cumbres Observatory telescope network of 0.4 m and 1.0 m telescopes ([Brown et al. 2013](#)) in the U , B , V , g , r , and i bands from the Global Supernova Project. The images were reduced using a PyRAF-based photometric reduction pipeline ([Valenti et al. 2016](#)). Apparent magnitudes were calibrated using the APASS catalog for g , r , and i and using Landolt standard fields observed with the same telescope on the same night for U , B , and V .

We used the ATLAS forced photometry service ([Tonry et al. 2018](#); [Smith et al. 2020](#)) to obtain further high-cadence photometry in two filters, cyan (c) and orange (o), which are roughly equivalent to Pan-STARRS filters $g + r$ and $r + i$, respectively.

Ultraviolet and optical images were obtained with the Ultraviolet/Optical Telescope (UVOT; [Romig et al.](#)

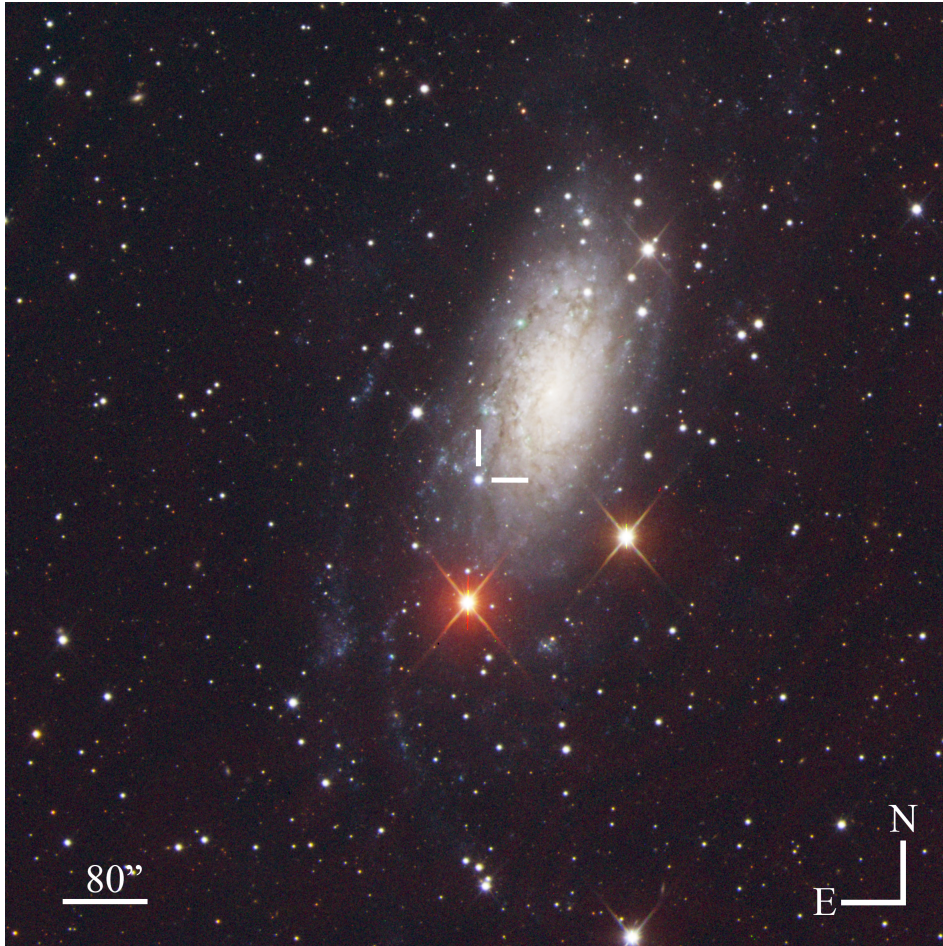


Figure 1. Composite gri image of SN 2024ggi and its host galaxy NGC 3621 taken by Las Cumbres Observatory on MJD 60412.46 (+1.7 days after the explosion).

2005) on the Neil Gehrels *Swift* Observatory (Gehrels et al. 2004) under a guest investigator program (PI: A. P. Ravi) that requested high-cadence (every ~ 6 hr) observations at early times. Further standard ToO requests to *Swift* at a more moderate cadence were obtained after several days. The UVOT images were reduced using the High-Energy Astrophysics software (HEASoft¹). The source region is centered at the position of the SN with an aperture size of $3''$ and the background is measured from a region without contamination from other stars with an aperture size of $5''$. Several epochs near the peak were observed with a faster readout setup (UVOT hardware mode: 0x0378) to mitigate saturation. Zero points for photometry were chosen from Breeveld et al. (2010) with time-dependent sensitivity corrections updated in 2020.

The complete early light curve from discovery until the SN is firmly on the plateau (MJD 60431.77) is shown in

Figure 2. A thorough analysis of the early photometry can be found in Section 4.

2.2. Spectroscopy

We present a log of spectroscopic observations in Table 2, and the full low-dispersion spectroscopic sequence is shown in Figure 3. Portions of our higher-resolution spectra are presented later in Section 5.2.

The first spectrum of SN 2024ggi was taken with the Yunnan Faint Object Spectrograph and Camera (YFOSC) on the Lijiang 2.4m telescope (Wang et al. 2019), which was used to classify it as a young SN II with flash-spectroscopy features (Zhai et al. 2024a; Zhang et al. 2024a). We have downloaded the public spectrum from the Transient Name Server to add to our analysis.

Multiple spectra were obtained with the Robert Stobie Spectrograph (RSS) on the Southern African Large Telescope (SALT; Smith et al. 2006), including one taken hours after the initial YFOSC spectrum exhibiting clear evolution in the flash features. The SALT data were

¹ <https://heasarc.gsfc.nasa.gov/docs/software/heasoft/>

Table 2. Log of Spectroscopic Observations

Date (UTC)	MJD	Telescope	Instrument	Phase (d)	Exp (s)
2024-04-11 14:35:47	60411.61	Lijiang 2.4m	YFOSC	0.81	1800
2024-04-11 23:31:08	60411.98	SALT	RSS	1.18	2393
2024-04-11 23:46:57	60411.99	Gemini-S	GMOS-S	1.19	300
2024-04-12 00:33:44	60412.02	Magellan-Clay	MIKE	1.22	300
2024-04-12 07:10:06	60412.29	Magellan-Clay	MIKE	1.49	300
2024-04-12 12:51:33	60412.53	COJ	FLOYDS	1.73	1800
2024-04-12 23:23:34	60412.97	SALT	RSS	2.17	2393
2024-04-13 05:15:11	60413.22	Bok	B&C	2.42	2100
2024-04-13 23:04:55	60413.96	SALT	HRS	3.16	1300
2024-04-14 05:26:54	60414.22	Bok	B&C	3.42	1400
2024-04-15 04:59:09	60415.21	Bok	B&C	4.41	1400
2024-04-16 06:46:05	60416.28	LCO Faulkes 2m	FLOYDS	5.48	600
2024-04-17 23:13:39	60417.97	SALT	RSS	7.16	1893
2024-04-19 22:40:23	60419.94	SALT	HRS	9.14	1300
2024-04-19 23:03:13	60419.96	SALT	HRS	9.16	1300
2024-04-20 06:00:18	60420.25	LCO Faulkes 2m	FLOYDS	9.45	600
2024-04-20 22:50:20	60420.95	SALT	RSS	10.15	1893
2024-04-21 07:36:22	60421.31	LCO Faulkes 2m	FLOYDS	10.51	600
2024-04-23 06:38:39	60423.27	LCO Faulkes 2m	FLOYDS	12.47	600

reduced using a custom pipeline based on the PySALT package (Crawford et al. 2010a).

Another early spectrum was obtained with the Gemini Multi-Object Spectrograph (GMOS; Hook et al. 2004; Gimeno et al. 2016) on the 8.1 m Gemini South Telescope using the B600 grating. Data were reduced using the Data Reduction for Astronomy from Gemini Observatory North and South (DRAGONS) package (Labrie et al. 2019), using the recipe for GMOS long-slit reductions. This includes bias correction, flat-fielding, wavelength calibration, and flux calibration.

Further spectra were obtained with the FLOYDS spectrographs (Brown et al. 2013) on the Las Cumbres Observatory’s 2m Faulkes Telescopes North and South (FTN/FTS) as part of the Global Supernova Project. One-dimensional spectra were extracted, reduced, and calibrated following standard procedures using the FLOYDS pipeline (Valenti et al. 2014).

We also include spectra taken with the Boller and Chivens (B&C) Spectrograph on the University of Arizona’s Bok 2.3 m telescope located at Kitt Peak Observatory, which were reduced in a standard way with IRAF (Tody 1986, 1993) routines.

Two sets of moderate- to high-resolution spectra were also taken. First, two epochs of echelle spectra were taken in a single night separated by 7 hours with the Magellan Inamori Kyocera Echelle (MIKE) double echelle spectrograph at the Magellan Clay Telescope at Las Campanas Observatory in Chile (Bernstein et al.

2003) with resolution of $R \approx 22,600$ for the red side (4900-9500 Å), and $R \approx 28,000$ for the blue side (3350-5000 Å). Pessi et al. (2024) have also presented an analysis of these two spectra. The spectra were reduced using the latest version of the MIKE pipeline using CarPy (Kelson et al. 2000; Kelson 2003). A barycentric velocity correction was applied to the data.

Another set of echelle spectra were taken with the SALT High Resolution Spectrograph (HRS; Crause et al. 2014) in moderate resolution mode ($R \approx 40,000$). These data were reduced with the standard MIDAS HRS pipeline², with steps including flat-fielding, wavelength calibration, and extraction (Kniazev et al. 2016, 2017). A barycentric velocity correction was applied to the data. We found that the Na I D lines from the HRS data are systematically shifted by -4 km s^{-1} compared to the MIKE data. As this is less than a resolution element, for consistency, we shift all the HRS data to the MIKE data for consistency.

3. LINE OF SIGHT EXTINCTION

We clearly detect Na I D absorption lines in our high-resolution spectra, which are known to correlate with interstellar dust extinction (Richmond et al. 1994; Munari & Zwitter 1997; Poznanski et al. 2012). As shown in Figure 4, there are components associated with Milky Way absorption for both Na I D1 and D2 lines. The Milky

² <https://astronomers.salt.ac.za/software/hrs-pipeline/>

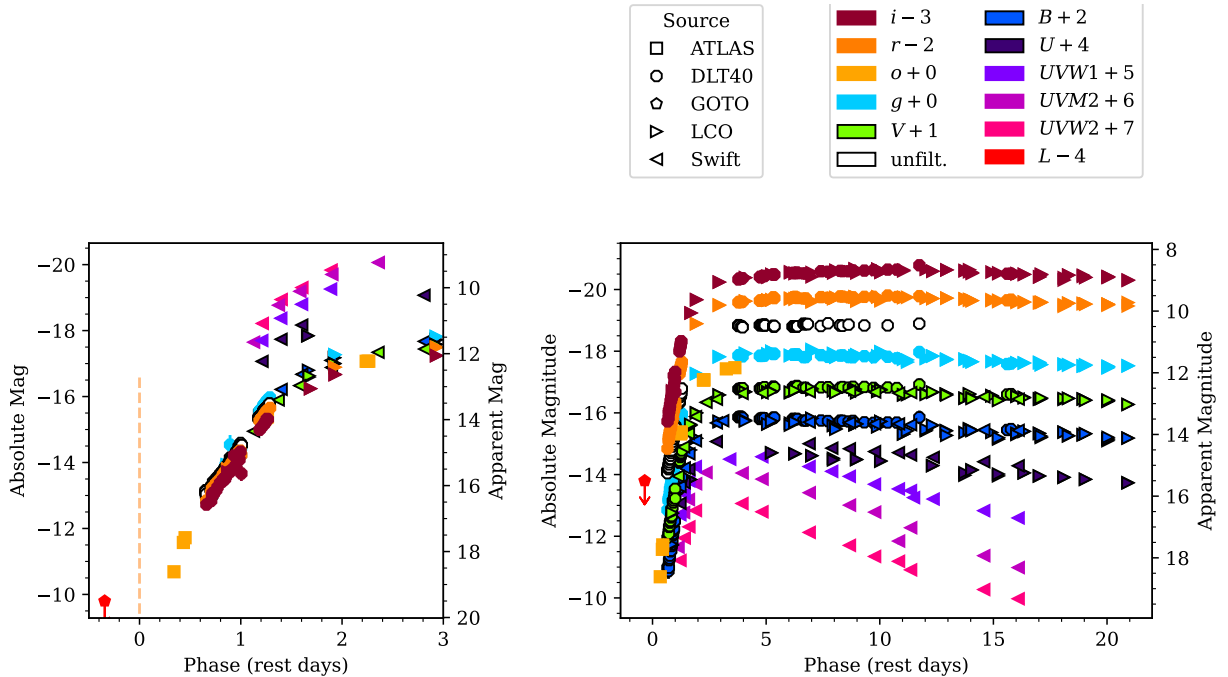


Figure 2. Left: Multiwavelength photometry of SN 2024ggi for the first 2.5 days in absolute and extinction-corrected (Milky Way + host) apparent magnitudes with no filter shifts. The dashed orange line represents the assumed explosion epoch. Right: The full multiwavelength light curve of SN 2024ggi extending to 21 days, including data from ATLAS, DLT40, Swift, Las Cumbres Observatory, and the last non-detection from GOTO (Killestein et al. 2024b). The data is well sampled throughout the first 20 days including the very early rise and plateau. (The data used to create this figure are available in the published article.)

Way absorption is composed of at least two component clouds, but we treat them as a single feature while calculating the equivalent width. In addition, there is another feature at $z = 0.00039$, which we interpret as another intervening cloud, as well as absorption features associated with the host galaxy. We calculated the equivalent width of Na I D1 and Na I D2 absorption features for the Milky Way, the intervening dust cloud, and the host galaxy using the `splot` task from IRAF for all five high-resolution spectra from MIKE and HRS. The equivalent width was used in Equation 9 of Poznanski et al. (2012) to calculate the color excess of each component, and a renormalization factor of 0.86 was applied following Schlafly & Finkbeiner (2011). From this calculation, we find $E(B - V)_{\text{MW}} = 0.054 \pm 0.020$, $E(B - V)_{\text{cloud}} = 0.066 \pm 0.020$, and $E(B - V)_{\text{host}} = 0.034 \pm 0.020$. The uncertainty in the derived extinction is dominated by the systematic uncertainty estimated by Poznanski et al. (2012). Note that the Milky Way value from Schlafly & Finkbeiner (2011) is $E(B - V)_{\text{MW}} = 0.0698$ mag, consistent with our Na I D-based measurement within the uncertainties. Thus the total extinction for SN 2024ggi is $E(B - V)_{\text{tot}} = 0.154 \pm 0.035$ mag, which we adopt for this paper. This value is consistent with values cal-

culated by Pessi et al. (2024) and Jacobson-Galán et al. (2024b).

4. LIGHT CURVE & COLOR EVOLUTION

The high cadence light-curve evolution of SN 2024ggi obtained by ATLAS, Swift, Las Cumbres, and DLT40 is presented in Figure 2 with the right panel showing all data up to +21 days with respect to our assumed explosion epoch. In the left panel, we focus on the light curve over the first 2.5 days. The peak absolute magnitude in the V band is -17.72 mag, 7 days after explosion on MJD 60417.8. In this section, we search for precursor emission at the SN position and explore the early light-curve and color evolution ($\lesssim 1-2$ d) with our extremely high-cadence data.

4.1. Precursor Search

It is clear that there is dense, confined CSM around many of the progenitors of SNe II (Förster et al. 2018; Khazov et al. 2016; Morozova et al. 2018; Bruch et al. 2021, 2023), indicating intense mass loss from the progenitor in the months to years before the explosion. This mass loss may produce observable precursor outburst activity. Precursors are commonly observed in SNe II_{in} (Ofek et al. 2014; Strotjohann et al. 2021), which are characterized by narrow hydrogen emission lines. In

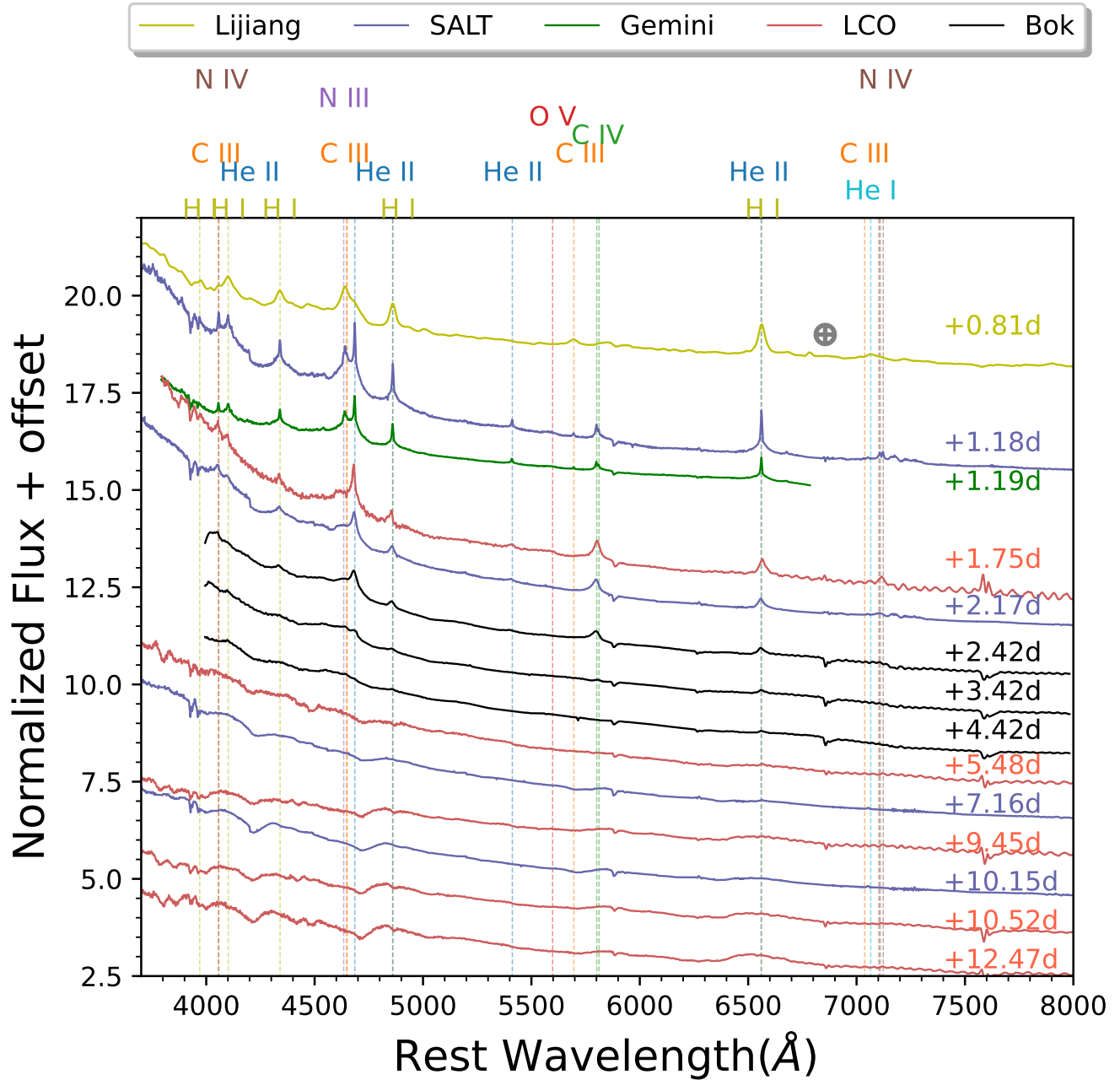


Figure 3. Optical spectral sequence of SN 2024ggi starting from +0.9 days (Zhai et al. 2024a) to +12.6 days after the explosion. Spectra from different instruments are indicated by different colors, as indicated in the legend, with the phases indicated on the right. The early spectra show flash features which disappear by roughly +3.5 days. All spectra will be made available on WISeREP (<https://www.wiserep.org>). (The data used to create this figure are available in the published article.)

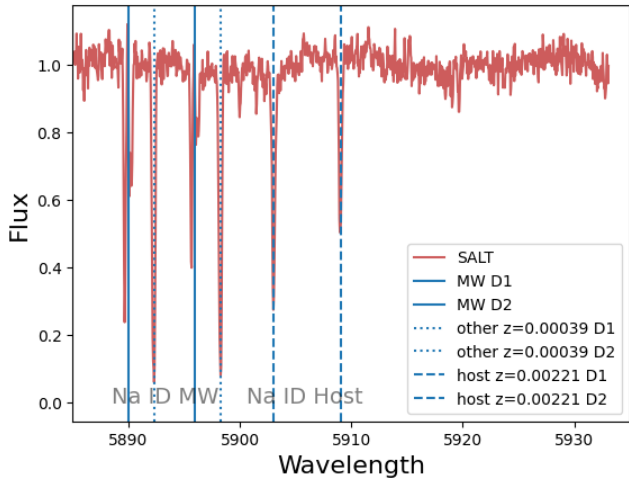


Figure 4. High-resolution data from SALT HRS observed on MJD 60413.96 (+3.16 days) focused on the Na I D lines of the host galaxy and Milky Way. There are six different absorption features corresponding to Na I D1 and D2 lines for the Milky Way, the host galaxy, and an intervening cloud, shown by blue lines for different redshifts. The total equivalent width of these lines measured from all the high-resolution spectra was used to calculate the extinction towards SN 2024ggi.

contrast, precursor emission has only been identified in one normal SN II (2020tlf; Jacobson-Galán et al. 2022). Other efforts to search for precursors in SNe II have yielded only nondetections (e.g., Johnson et al. 2018), including for the nearby SN 2023ixf, whose pre-SN site had been observed for many years by several major surveys (Neustadt et al. 2024; Hiramatsu et al. 2023a; Dong et al. 2023; Ransome et al. 2024; Rest et al. 2024).

The position of SN 2024ggi has been monitored by ATLAS since 2017. We obtained forced photometry at the SN site from the ATLAS forced photometry server (Shingles et al. 2021), which was then stacked in windows of 15 days to achieve deeper limits using the method presented in Young (2022). We adopted a signal-to-noise threshold of 3 for source detections and a signal-to-noise threshold of 5 for calculating the upper limits, as recommended by Masci (2011). The results are presented in Figure 5. Therefore, we conclude that precursor emission is not detected for SN 2024ggi down to ~ -9 mag.

If there were precursor activities for SN 2024ggi, they would have to be faint and only last for a short duration. Although the nondetection of precursors for SN 2024ggi is not as deep as that for SN 2023ixf, it is still ~ 2 mag deeper than the precursor detected in SN 2020tlf. The diversity of precursor activities observed in these SNe suggests that multiple physical mechanisms are respon-

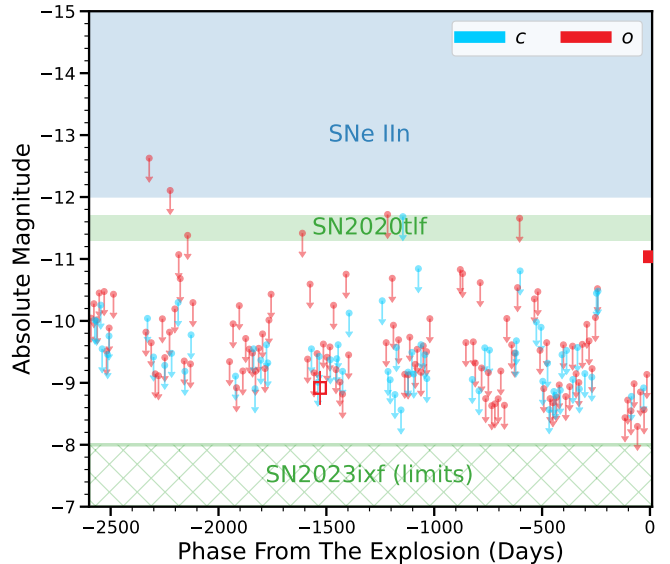


Figure 5. Nondetection limits on the pre-explosion activity of SN 2024ggi. The typical brightness of pre-explosion outbursts of SNe IIn is indicated by the blue area (Ofek et al. 2014; Strotjohann et al. 2021). The brightness of precursor emission observed in Type II SN 2020tlf is marked with the green area (Jacobson-Galán et al. 2022), while the nondetection limit on the pre-explosion activity of Type II SN 2023ixf is represented by the green hatched area (Dong et al. 2023; Ransome et al. 2024; Rest et al. 2024).

sible for the dense and confined CSM around the progenitors of SNe II, as suggested by Dong et al. (2023).

4.2. Temperature & Radius

We construct a bolometric light curve using the multi-band photometry obtained for SN 2024ggi. During these earliest phases, the spectral energy distribution (SED) peaks in the near-UV, so Swift observations are required to get a valid measurement of temperature (Arcavi 2022). Therefore, to assemble single-epoch SEDs, we group our Swift photometry into bins of ~ 6 hours during the first day of Swift observations and bins of ~ 1 day thereafter, each of which includes at least one filter with a shorter effective wavelength than U . Then we add $BVgri$ points by linearly interpolating our high cadence ground-based data. We then fit a blackbody spectrum to each of these single-epoch SEDs using the Light Curve Fitting package (Hosseinzadeh et al. 2023) to derive a temperature and photospheric radius. These are shown in Figure 6. We find the temperature on +1.2 days to be 24.9 ± 1.9 kK, which peaks at 30.7 ± 1.5 kK at +1.4 days. The temperatures found here are consistent with temperatures found by Jacobson-Galán et al. (2024b) and slightly higher at the peak than Chen et al. (2024), where they do not include UV data for the temperature calculations. The peak temperature for SN 2024ggi is

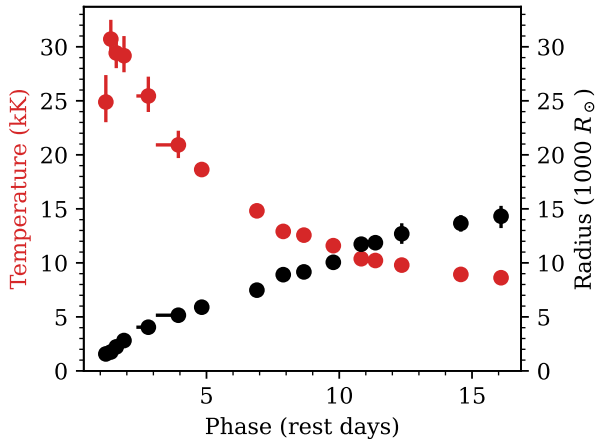


Figure 6. Temperature (red) and photospheric radius (black) evolution of SN 2024ggi derived from fitting a blackbody SED to the multiband photometry.

close to the temperature observed for SN 2023ixf (34.3 kK) by Zimmerman et al. (2024). The implied radius at the first epoch is $1571 \pm 156 R_{\odot}$ which is smaller than the radius calculated for SN 2023ixf of $2731 R_{\odot}$ by Zimmerman et al. (2024).

4.3. Rapid Evolution on the First Day

In the first ~ 0.5 – 1.5 d after explosion, we collected a nearly continuous set of light-curve data, with ~ 30 data points in each of the B , V , g , r , i , and Clear/Open bands in that time frame. This early evolution began when the SN was still very faint, with $M_V \approx -12.75$ mag. In addition to the SED fitting described in the previous section, we fit a blackbody SED to each epoch of high-cadence filtered photometry using an MCMC routine implemented in Light Curve Fitting package (Hosseinzadeh et al. 2023) and then construct a pseudobolometric light curve by integrating the SED between the U and I bands. Since the UV data in earlier phases is limited, we only consider the luminosity between U and I for consistency. This approach facilitates comparisons to previous optical-only data sets.

When we zoom in on the first day of our pseudobolometric light curve, as shown in Figure 7, there is a clear change of slope from the first few hours to the end of the first day. We note that we see this change in slope for all the individual filters. This deviation in the early light curve has also been seen in the case of SN 2023ixf (see Figure 2 in Hosseinzadeh et al. 2023). We fit a broken power law to this pseudobolometric light curve from $+0.6$ to $+1.3$ days. The first set of data spanning up to $+1.0$ days is best fit by a power law with $\alpha_1 = 3.63$ (red; Figure 7). After that, we see an increase in the slope which is best fit by $\alpha_2 = 4.67$ (blue; Figure 7).

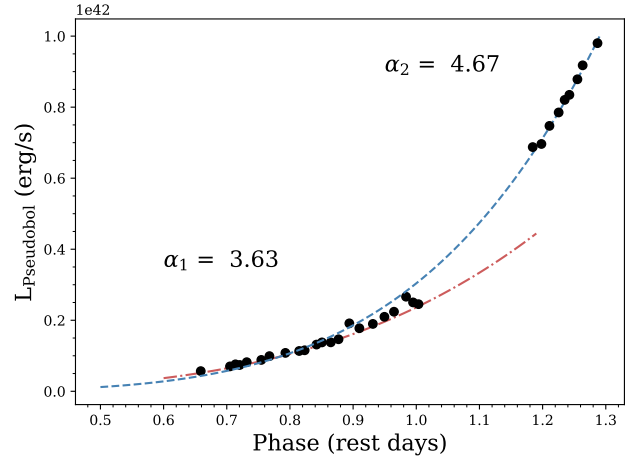


Figure 7. Pseudobolometric light curve of SN 2024ggi for the first $\lesssim 1.3$ days after the explosion. There is a clear evolution in the slope of the luminosity increase in a short period of time. We fit two different power laws to the data set. The very early data is best fit by a power-law index of 3.63 and the second set by a power-law index of 4.67. These fits are shown as solid red and blue lines for each set of data.

This change in power-law index is clearly visible both in the pseudobolometric light curve and individual filters. The initial power-law index is close to the values derived by Pessi et al. (2024). However, they do not witness the second part of the light curve rise. This change in slope could be due to the change in the density of CSM where the initial higher density slows down the rise in luminosity and this increases when the density is lower.

4.4. Color evolution

We examined the early color evolution of SN 2024ggi with a high-cadence multiwavelength data set. In Figure 8, we present the extinction-corrected $B - V$ plot with respect to phase. During the first few hours, the color gets rapidly bluer. We note that we see similar evolution in other filters such as $r - i$ and $g - r$ as well. Then at roughly 2 days post-explosion, we reach a blue maximum, after which the color then starts to trend redward.

We see that the flash features in spectra coincide with blueward color evolution. Once the color starts evolving redward, the narrow emission lines indicative of CSM interaction disappear. Similar color behavior has been seen previously in SN 2023ixf (Hiramatsu et al. 2023b; Li et al. 2024; Teja et al. 2023) and SN 2018zd (Hiramatsu et al. 2021). The turnover in color evolution from blueward to redward happens later in SN 2023ixf than in SN 2024ggi, but this is closer to the time at which flash features disappear for SN 2023ixf ($+7$ days). Therefore, we attribute the initial blueward color evolution to

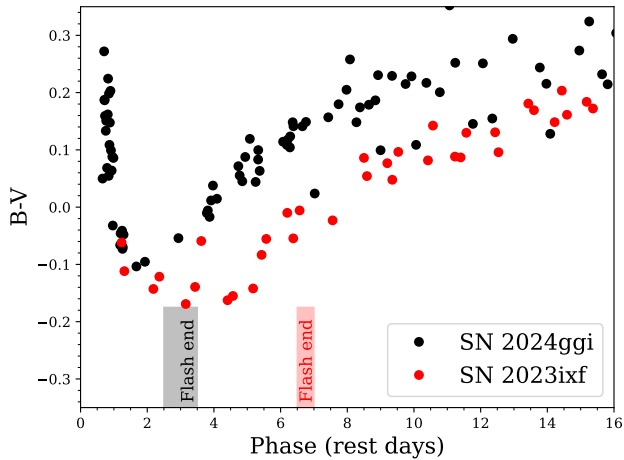


Figure 8. Extinction corrected B-V color curve of SN 2024ggi (black) and SN 2023ixf (red) for the first 16 days. The last epoch where spectra have flash features for both SN 2024ggi (black) and SN 2023ixf (red) are indicated by the shaded regions. The extent of the shaded region is the length of time between the last spectrum showing a flash feature and the first spectrum with no flash features. The data at phases before 2 days show the color is getting bluer quickly prior to evolving redward. (The data used to create this figure are available in the published article.)

interaction with dense CSM or delayed/extended shock-breakout in the CSM (e.g. Chugai et al. 2004; Smith & McCray 2007; Ofek et al. 2010; Dessart et al. 2017a; Haynie & Piro 2021). Hiramatsu et al. (2021) likewise interpreted early blueward color evolution in SN 2018zd as a delayed shock breakout through dense CSM, which can provide an additional power source for the explosion and hence a bluer color as the shock front propagates through the CSM.

4.5. Shock cooling model

In the absence of significant CSM interaction, the early photometric evolution of SNe II is assumed to be driven by cooling emission from the shock-heated ejecta. A series of increasingly complete prescriptions by Sapir et al. (2011, 2013), Rabinak & Waxman (2011), Katz et al. (2012), Sapir & Waxman (2017), and Morag et al. (2023, 2024) model the shock-cooling emission as a function of the properties of the progenitor star and the explosion, in particular the stellar radius. Here, we adopt the model of Morag et al. (2023, hereafter MSW23), which builds on the model of Sapir & Waxman (2017) by accounting for the very early “planar” phase, where the thickness of the emitting shell is smaller than the stellar radius, and for some line blanketing in UV. This model has been applied to a sample of SNe II observed by the Zwicky Transient Facility and Swift (Irani et al. 2023),

as well as several nearby supernovae with very high-cadence early observations (Hosseinzadeh et al. 2023; Andrews et al. 2024; Meza Retamal et al. 2024; Shrestha et al. 2024), with mixed results. These previous works have concluded that the model does not perform well when there is strong circumstellar interaction, which is likely the case here. We note that SN 2024ggi shows signs of CSM interaction but there is value in performing this modeling, which can be used to compare to those cases where SN without CSM interaction is apparent. This can provide crucial knowledge on how CSM interaction affects the light curves and our understanding of shock cooling.

We fit the model of MSW23 to the early light curve of SN 2024ggi using a Markov Chain Monte Carlo (MCMC) routine implemented in the Light Curve Fitting package (Hosseinzadeh et al. 2023). The priors and best-fit values for each parameter are tabulated in Table 3, and the best-fit model is plotted in Figure 9. We use observed data from 60411 to 60417 MJD which is the range of time the best-fit model is valid following the prescription described in Appendix of Morag et al. (2023) (Equation A3). The model could not fit the data from the first 24 hours, which has been seen for SN 2023ixf (Hosseinzadeh et al. 2023). However, for the rest of the data we find that the model converges and gives an overall good fit. The best-fit model gives the explosion epoch to be $60411.947^{+0.008}_{-0.058}$ MJD, which is after the discovery date (60411.65 MJD), due to the code not being able to model the early data points. We also ran the shock cooling model by forcing the upper limit for the explosion epoch to be the discovery date. However, this run was not able to provide a good fit for any part of the light curve. Thus, we pick the model that converges to calculate our parameters. The progenitor radius from the best-fit model is found to be $431^{+14}_{-215} R_{\odot}$. However, we caution that this is not physically representative of the stellar radius due to the extended shock break out observed in the <1d light curve, which is unable to be fit by the model.

5. SPECTROSCOPY

5.1. Spectral evolution and line identification

We present a high cadence, low-resolution spectral sequence of SN 2024ggi in Figure 3 starting from +0.81 days to +12.6 days with respect to our estimated explosion epoch. The early spectra contain clear flash ionization features indicating the recombination of the CSM ionized by the shock-breakout and ongoing interaction between the ejecta and dense CSM (Gal-Yam et al. 2014; Khazov et al. 2016; Yaron et al. 2017; Tartaglia et al. 2021; Bruch et al. 2021; Hiramatsu et al. 2021; Terreran

Table 3. Shock-cooling Parameters

Parameter	Variable	Prior			Best-fit Values ^a	Units
		Shape	Min.	Max.		
Shock velocity	v_{s*}	Uniform	1	5	$1.7_{-0.2}^{+0.4}$	$10^{8.5} \text{ cm s}^{-1}$
Envelope mass ^b	M_{env}	Uniform	0	10	$0.9_{-0.3}^{+0.7}$	M_{\odot}
Ejecta mass \times numerical factor	$f_{\rho}M$	Uniform	0.05	100	50 ± 40	M_{\odot}
Progenitor radius	R	Uniform	0	2000	431_{-215}^{+14}	R_{\odot}
Explosion time	t_0	Uniform	60410.0	60413.14	$60411.947_{-0.058}^{+0.008}$	MJD
Intrinsic scatter	σ	Log-uniform	0	10^2	$30.1_{-0.8}^{+1.1}$...

^aThe ‘‘Best-fit Values’’ columns are determined from the 16th, 50th, and 84th percentiles of the posterior distribution, i.e., median $\pm 1\sigma$.

et al. 2022; Bostroem et al. 2023; Bruch et al. 2023; Jacobson-Galán et al. 2023; Hiramatsu et al. 2023b). First, we use our SALT RSS spectrum from 60411.979 MJD (+1.18 days) for line identification as it has a higher signal-to-noise ratio than the classification spectrum from the Lijiang 2.4m telescope (Zhai et al. 2024b). We clearly detect lines of different ionization levels including He II $\lambda 6559.8$, C III $\lambda 5695.9$, C IV $\lambda \lambda 5801.3$, N III $\lambda 4858.82$, He II $\lambda 4685.5$, N III $\lambda 4640.64$, N III $\lambda 4097.33$, N IV $\lambda \lambda 4057.76$, O V $\lambda 5597.91$, and N IV $\lambda \lambda 7109$. Compared to the first spectra at +0.81 days, we see a development of high ionization state lines such as C IV and O V in the +1.18 and +1.19 day spectra. This implies there is an increase in temperature during this phase which is consistent with the temperature and color evolution as shown in Figure 6 and Figure 8 respectively. These narrow emission features only persist for a few days, and the spectrum from Bok at +3.42 days is almost featureless. The N III $\lambda 4640.64$ line is only visible for ~ 9 hours, with the strongest emission seen in the first spectrum. Similarly the N III $\lambda 4097.33$ and N IV $\lambda 4057.76$ lines disappear within a day from the first observation. We identify O V $\lambda 5597.91$, a rare feature in flash spectra, in three different spectra taken at +1.18, +1.19, and +1.75 days, which is consistent with the identification in Jacobson-Galán et al. (2024b).

The rest of the lines persist until +3.42 days. On day +5.48, there is a clear broad absorption feature present in H β from which we estimate the ejecta velocity to be $\sim 9000 \text{ km s}^{-1}$ based on the minimum absorption trough. We use this velocity, along with the duration of the flash features (3.42 days) to compute an approximate CSM radius of $R_{\text{CSM}} \sim 2.7 \times 10^{14} \text{ cm}$. This value for the approximate CSM radius is consistent with that of Jacobson-Galán et al. (2024b) to within a factor of two. Using the value for R_{CSM} and assuming a canonical wind velocity of $v_w \approx 10 \text{ km s}^{-1}$ (Deutsch 1956) we find that

the mass loss began ~ 9 years before explosion. If instead we assume a velocity of $v_w = 37 \pm 4 \text{ km s}^{-1}$ derived from the early high-resolution spectra of SN 2024ggi, which is discussed in the next section, we find that the mass loss began just ~ 2 years before the explosion. Note, we do not see any precursor activity 2 years before the explosion in ATLAS forced photometry data as shown in Figure 5.

5.2. High-resolution spectroscopy

We obtained high-resolution spectra of SN 2024ggi using MIKE on the Magellan-Clay telescope on MJDs 60412.015 and 60412.29, or +1.2 and +1.5 days after the explosion, respectively. In addition, we acquired high-resolution spectra from HRS on SALT on MJDs 60413.96 (+3.16 d), 60419.94 (+9.14 d), and 60419.96 (+9.16 d). We clearly see the Ca II H & K and Na I D absorption features in all of our high-resolution spectra both from MIKE and SALT (see Figure 4). We utilized the equivalent width of Na I D1 and Na I D2 lines from the host and the Milky Way to calculate the extinction in Section 3. In addition, we found the host Na I D lines are at a redshift of 0.00221, which we adopt as the host redshift for this paper (Table 1). Note that this value is slightly offset from the reported redshift of NGC 3621 itself, although it is consistent with the expected rotation curve of the galaxy (Pessi et al. 2024).

In our early high-resolution data from MIKE, we identify narrow emission lines associated with the flash ionization which clearly evolve over the ~ 7 hours between them.

A close examination of the H α emission line is shown in Figure 10 (left). The fading in H α is clear. A weak absorption P Cygni feature is also apparent in both spectra, which we associate with the RSG wind material prior to explosion. We find the velocity of the absorption feature with respect to the peak of the emission to be at

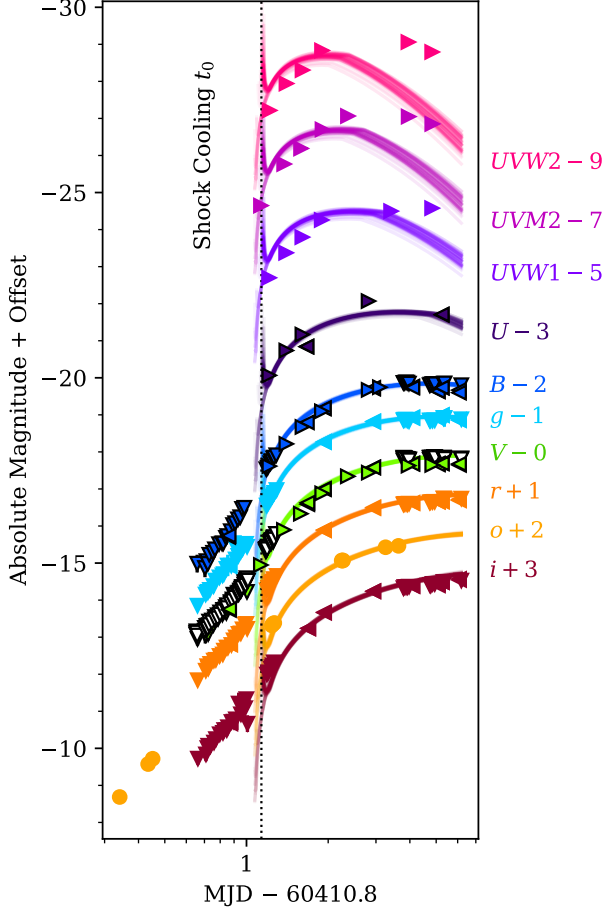


Figure 9. Shock-cooling modeling of SN 2024ggi using the prescription of Morag et al. (2023). The model does a good job fitting the rise after the first day of data to the maximum for all filters and the initial plateau for optical filters of SN 2024ggi but does not correctly estimate the explosion time, with SN emission apparent a full day before the model’s preferred explosion epoch. Similar behavior and mismatch to the model were seen in the case of SN 2023ixf (Hosseinzadeh et al. 2023).

$-37 \pm 4 \text{ km s}^{-1}$. We also fit a Gaussian to the narrow emission line of $\text{H}\alpha$ in both MIKE epochs to calculate the full-width-half-maximum (FWHM), which we find to be 36.9 km s^{-1} and 37.0 km s^{-1} , respectively. The velocities from both methods are very similar, and we therefore assume $37 \pm 4 \text{ km s}^{-1}$ as the RSG wind/CSM velocity. We note this value is different from the 79 km s^{-1} calculated by Pessi et al. (2024), using the same MIKE data, where they evaluate CSM velocity using the blue shift they observe for the $\text{H}\alpha$ feature.

We overall find all the lines in the first two spectra from MIKE to be offset from the rest wavelength by -75 km s^{-1} , after utilizing the Na I D-based host red-

Table 4. Line Strengths from High Resolution Spectra

Line	λ (\AA)	EW (\AA)	
		+1.22 days	+1.49 days
$\text{H}\alpha$	6562.7	1.61 ± 0.12	0.47 ± 0.05
C IV	5811.98	1.06 ± 0.07	1.38 ± 0.09
C IV	5801.3	1.78 ± 0.09	2.61 ± 0.09
He II	4685.5	1.29 ± 0.03	0.49 ± 0.03
C III	4650	0.15 ± 0.04	0.04 ± 0.02
C III	4647.5	0.21 ± 0.05	0.18 ± 0.06
N III	4640.64	0.78 ± 0.08	0.28 ± 0.11
N III	4634	0.32 ± 0.07	0.11 ± 0.01

shift as described above (see Figure 10, right). In addition, we identify high-ionization lines such as N III, C III, He II, C IV, He II, and $\text{H}\alpha$ in our first two spectra which are shown in Figure 11. In Figure 11, we have shifted the spectra by -75 km s^{-1} to align with the rest wavelengths of these lines, shown by the dashed lines. We find that the strengths of the lines change significantly in the 6.6 hours between exposures (see the black and red lines in Figure 11). We measured the equivalent widths of these lines, and they are listed in Table 4. For the C IV line we find the strength increases between the two observation which indicates an increase in ionization and temperature. The rest of the lines show a decrease in strength with time.

We have a SALT HRS spectrum at +3.16 days, which is towards the end of the phase where we see flash features in low-resolution spectra. Hence, we carefully inspected the high-resolution spectrum looking for any faint and persistent narrow emission lines. We do see a weak, narrow $\text{H}\alpha$ line, but due to the low signal-to-noise ratio, we could not perform a quantitative analysis. However, we did not see any other features present in this spectrum. We also do not see any narrow emission lines in the SALT HRS spectra at +9.14 and +9.16 days, which agrees well with the behavior seen in low-resolution spectra at similar phases.

5.3. Comparison with models

Variations in mass-loss rate, SN luminosity, surface abundance, and CSM density profile can all affect the characteristics and evolution of flash-spectroscopy features. Here we compare our low-dispersion spectroscopic data set to two available model grids by Dessart et al. (2017b) and Boian & Groh (2019) to infer the properties of the progenitor star and its CSM.

5.3.1. Boian & Groh

Boian & Groh (2019) used the radiative transfer code CMFGEN (Hillier & Miller 1998; Hillier & Dessart 2012;

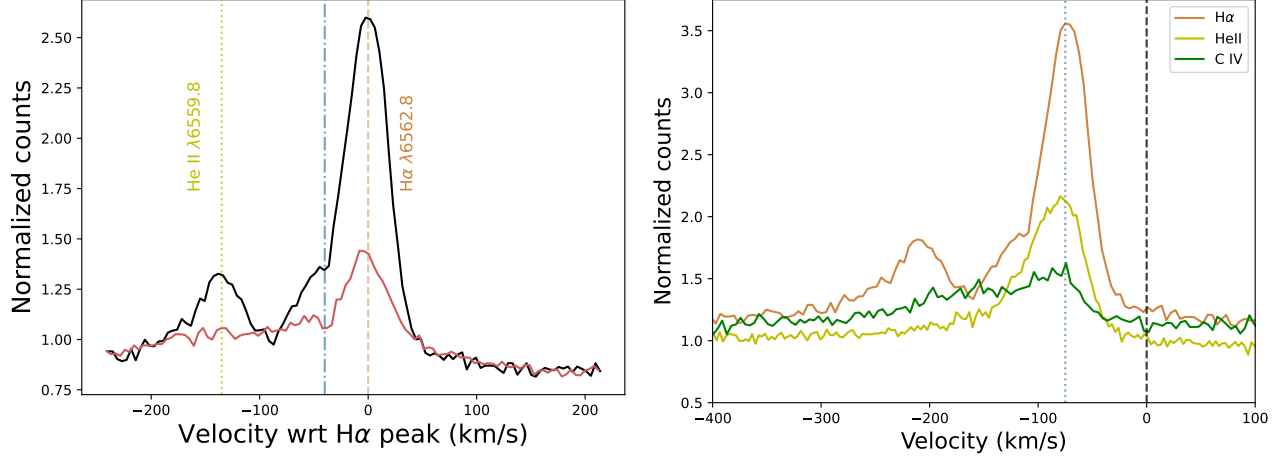


Figure 10. Left: High-resolution MIKE data +1.22 days (black) and +1.49 days (red) focusing on the $H\alpha$ feature. The brown dashed line represents the peak of the feature. We calculate a velocity relative to this wavelength at the position of the shallow absorption feature, a P Cygni signature. The dashed blue line is placed at the shallow absorption feature at $-37 \pm 4 \text{ km s}^{-1}$, which we use as one of the markers for CSM velocity. He II is also identified by the yellow dashed line. Right: Line profiles of $H\alpha$, He II $\lambda 4685.5$, and C IV from the first epoch (+1.22 days), where the black dashed line represents the rest wavelength of these lines. We see a shift in velocity of -75 km s^{-1} for all of the lines, shown by the blue dotted line.

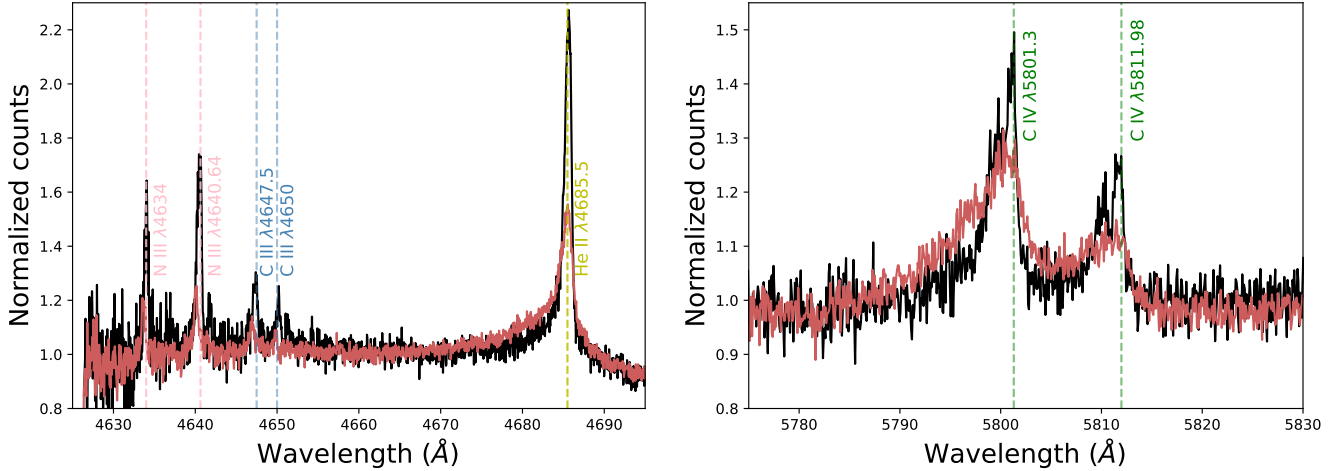


Figure 11. The two panels show narrow emission lines identified in high-resolution MIKE data from the first (black; +1.22 days) and second (red; +1.49 days) epochs. The spectra are shifted by -75 km s^{-1} to clearly indicate the narrow emission lines. In the first panel, there are N III, C III, and He II lines identified by pink, blue, and yellow dashed lines, respectively. The second panel zooms in on the C IV lines. The lines evolve rapidly within a few hours between the two epochs.

Dessart et al. 2013; Hillier & Dessart 2019) to create an extensive spectral library that simulates the interaction of a SN with CSM. They model early spectra approximately one day after explosion with a mass-loss rate ranging from $\dot{M} = 5 \times 10^{-4} - 10^{-2} M_{\odot} \text{ yr}^{-1}$, SN luminosities $L = 1.9 \times 10^8 - 2.5 \times 10^{10} L_{\odot}$, and three different surface abundances corresponding to He-rich abundance representing an LBV/WN/stripped star, CNO-processed abundance for high-mass RSG/BSG/YSG, and the solar abundance representing a low-mass RSG. They make use of the identification of various lines from

highly ionized species to low ionization in an early spectrum of SNe interacting with their CSM to map the progenitor properties. These lines are shown in Figure 12. We visually inspected the spectral library created by Boian & Groh (2019) to find the most similar spectrum to our earliest SALT RSS spectrum at +1.18 days after the explosion of SN 2024ggi.

The first SN 2024ggi spectrum observed by SALT at +1.18 days shows flash features including clear lines for He II ($\lambda 4685.5, 4860, 5412, 6559.8$), N IV ($\lambda 4058, \lambda \lambda 7109, 7122$), N III ($\lambda \lambda 4634, 4640$), C III

($\lambda\lambda 4647, 4650$), and C IV ($\lambda\lambda 5801, 5811$). For different abundance cases, the only model with clear N III, He II, and N IV are seen for $L = 1.5 \times 10^9 L_\odot$ and $\dot{M} = 3 \times 10^{-3} M_\odot \text{ yr}^{-1}$. The model that matches best with the observed spectrum is shown in Figure 12 where many of the features match. However, across the full spectrum, none of the observed lines have the right intensity compared to the models. From this model we calculate a mass-loss rate of $\dot{M} = 4 \times 10^{-3} M_\odot \text{ yr}^{-1}$, after scaling for the difference in luminosity between the model and the observations, as described in Boian & Groh (2019) and find $L = 2.3 \times 10^9 L_\odot$ for SN 2024ggi.

5.3.2. Dessart & Hillier models

We also visually compared the early spectra of SN 2024ggi with the CMFGEN radiation hydrodynamics model by Dessart et al. (2017b). These simulations model the spectroscopic signatures of RSG explosions enshrouded in a CSM out to $\sim 5\text{--}10 R_\odot$ and mass $\leq 10^{-1} M_\odot$. All of the models have the same stellar radius of $501 R_\odot$ except for **r2w1**. The mass-loss rate varies from $10^{-6} M_\odot \text{ yr}^{-1}$ to $10^{-2} M_\odot \text{ yr}^{-1}$. We visually inspected the simulated spectra from the different models with our data from SALT at +1.18 days after the explosion. In our spectrum, we see flash features described above, which are only present past a few hours in the higher mass-loss rates Dessart et al. (2017b). We do not find any model that reproduces all of the observed features in the SN 2024ggi spectra. We identify a N III line next to He II which is only present for the **r1w4** case as seen in Figure 13. However, we also identify C IV and N IV lines in the observed spectrum at +1.18 days. These lines disappear by +1 day in the **r1w4** model while they are present in **r1w6** until day +3. Thus, we do not find one model that reproduces the observations, but the best fits generally favor a higher-mass-loss model. In addition, the observed spectral evolution diverges significantly from the models starting +2.0 days as the models evolve rapidly and develop absorption features in $\text{H}\alpha$, which is not seen in our observed spectra. The mass-loss rates for **r1w4** and **r1w6** are $10^{-3} M_\odot \text{ yr}^{-1}$ and $10^{-2} M_\odot \text{ yr}^{-1}$, respectively. This mass-loss-rate range is similar to the value we find from our comparison to the Boian & Groh (2019) model of $\dot{M} = 4 \times 10^{-3} M_\odot \text{ yr}^{-1}$ as shown in Figure 12. Jacobson-Galán et al. (2024b) compared their spectra with models from Jacobson-Galán et al. (2024c) and found the most compatible model to give a mass loss rate of $10^{-2} M_\odot \text{ yr}^{-1}$. This mass loss rate is comparable to the rate we find by comparing to Dessart et al. (2017b) and Boian & Groh (2019) models.

6. COMPARISON WITH SN 2023IXF

SN 2023ixf, the recent SN in M101, is a well-studied SN II with flash features at a similar distance to SN 2024ggi. We compare the photometric and spectroscopic behavior of these two SNe in this section.

First, the light curve in the first 24 hours for both SNe are not described by the simple function $F \propto T^2$, where F is flux and T is time, as might be expected in an “expanding fireball” scenario (Hosseinzadeh et al. 2023; Hiramatsu et al. 2023a). Hiramatsu et al. (2023a) find that variable mass loss could explain this non-monotonic rise in SN 2023ixf. The shock-cooling model by Morag et al. (2023) was also not able to match the full rise of the early data before the Itagaki (2023) discovery, as shown by Hosseinzadeh et al. (2023). This is similar to what we found for SN 2024ggi. In addition, at comparable phases, the light curve of SN 2024ggi rises faster than that of SN 2023ixf, as shown in Figure 14. This difference could be explained by the details of the CSM density profile and extent between the two SNe, which may be further corroborated by the narrow emission lines of SN 2024ggi disappearing faster than for SN 2023ixf (+3.4 vs +7 days). Both SNe show blueward evolution in the very early phase (Figure 8), which may be due to the initial shock breakout inside dense CSM. This blueward color evolution roughly coincides with the phases where flash features are seen in the spectra, as shown by the gray and red shaded region in Figure 8. Overall SN 2023ixf remains bluer than SN 2024ggi for the first 16 days, as shown in Figure 8. This again could be explained by the CSM interaction lasting longer for SN 2023ixf than for SN 2024ggi.

We compare the spectral evolution of SN 2024ggi with SN 2023ixf as shown in Figure 15. We find all the lines present in SN 2023ixf are also in SN 2024ggi. However, in the very first spectrum of SN 2024ggi, we identify C III $\lambda 5695.9$ and O V $\lambda 5597.91$, which is not seen in SN 2023ixf. We find that the narrow emission lines in SN 2024ggi disappear faster than in SN 2023ixf, and by +3.42 days, all of the narrow emission lines from SN 2024ggi have disappeared, whereas for SN 2023ixf the lines vanish at +7 days (Bostroem et al. 2023; Jacobson-Galán et al. 2023, 2024b; Hiramatsu et al. 2023b). However, for both cases, we get a similar mass loss rate between 10^{-3} and $10^{-2} M_\odot \text{ yr}^{-1}$ (Bostroem et al. 2023) when compared to theoretical models by Boian & Groh (2019) and Dessart et al. (2017b). Since we find similar mass loss rates for both events, this extended presence of flash features of SN 2023ixf could be due to CSM produced by the progenitor extending farther than the CSM surrounding SN 2024ggi, indicating a different mass-loss history of the progenitor. Even though the mass-loss rates are similar, the smaller CSM

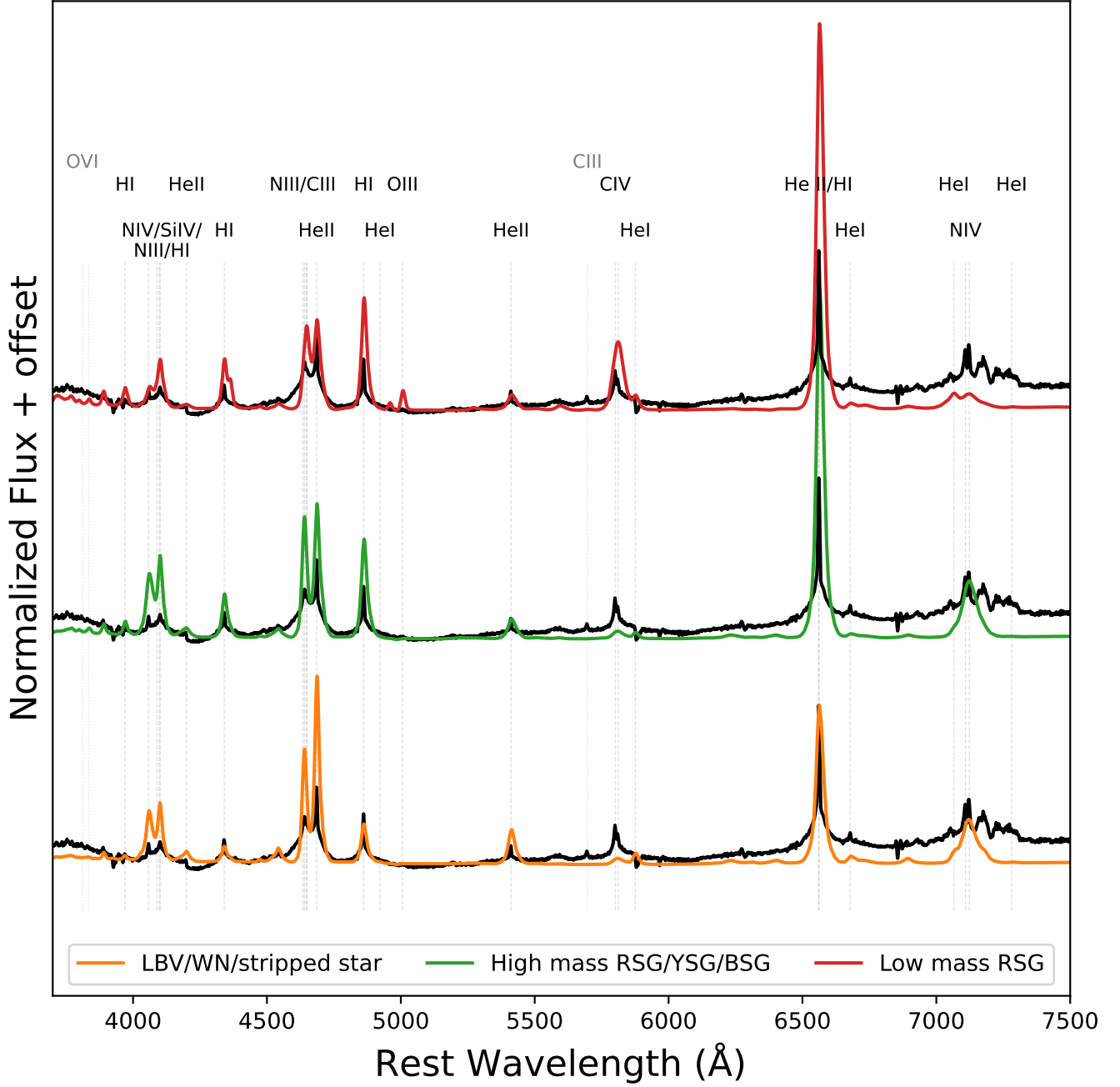


Figure 12. Comparison of our +1.27 days spectrum (black) to [Boian & Groh \(2019\)](#) models with $L = 1.5 \times 10^9 L_{\odot}$ and $\dot{M} = 3 \times 10^{-3} M_{\odot} \text{ yr}^{-1}$ for three different abundances. The orange line shows the He-rich abundance representing an LBV/WN/stripped star, the green line is for high-mass RSG/BSG/YSG with CNO-processed abundance, and the red is for solar abundance representing a low-mass RSG. Vertical lines represent the ions that are used as a diagnostic of the progenitor in [Boian & Groh \(2019\)](#). The model spectra have been convolved with a Gaussian kernel to mimic the resolution of the observed spectrum.

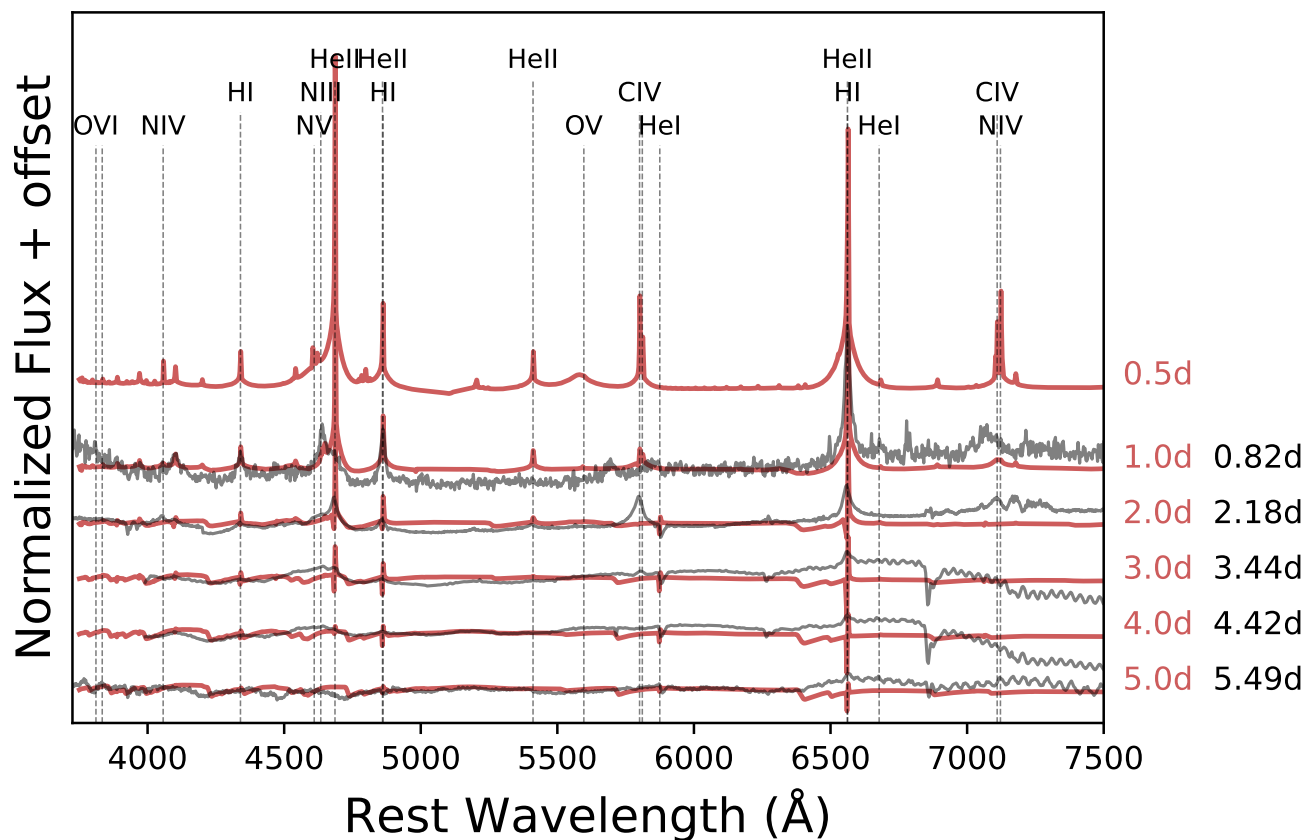


Figure 13. Comparison of SN 2024ggi spectra (black) with `r1w4` model (red) from Dessart et al. (2017b). The observational and model epochs are shown in their respective colors on the right. This is the only model that has the N III line, which is present in the observed spectrum. Thus, we present this model as the best representation of the observed spectrum. However, the model spectra evolve faster than the observed spectra of SN 2024ggi. This difference in evolution was also seen for SN 2023ixf (Bostroem et al. 2023).

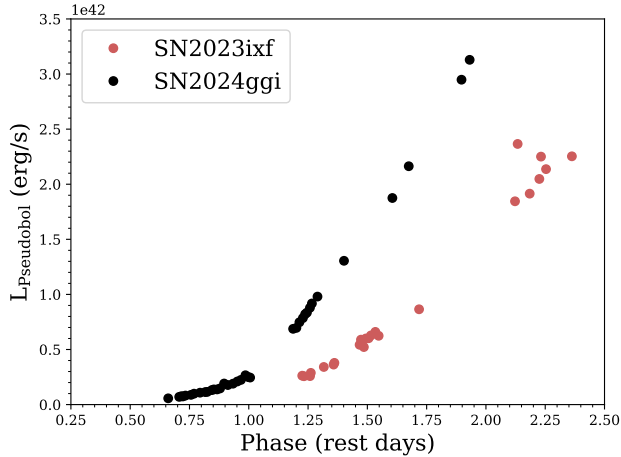


Figure 14. Pseudobolometric light curve of SN 2024ggi (black) compared to SN 2023ixf (red) from Hosseinzadeh et al. (2023), excluding data from amateur astronomers for the first +2.5 days after the explosion. The rise in luminosity for SN 2024ggi is faster than the rise observed for SN 2023ixf.

radius in SN 2024ggi implies that it has a lower total mass of CSM compared to SN 2023ixf.

From high-resolution spectroscopy, we calculate the CSM velocity of SN 2024ggi to be $37 \pm 4 \text{ km s}^{-1}$, which is similar to a typical quiescent RSG wind of $20\text{--}30 \text{ km s}^{-1}$ (Jura & Kleinmann 1990). Though the calculated CSM velocity is typical for RSG winds, we note that radiative acceleration could contribute to this velocity. The wind speed of SN 2024ggi is lower than the velocity of 115 km s^{-1} calculated by Smith et al. (2023) for SN 2023ixf where they mention that this higher velocity could be due to the radiation acceleration. Utilizing high-cadence mid-resolution spectroscopy, Zhang et al. (2023) observed that the velocity of SN 2023ixf increased from 55 km s^{-1} at $t \approx 1.8 \text{ d}$ to 141 km s^{-1} at $t \approx 3.0 \text{ d}$. Furthermore, Zhang et al. (2024a) found that the observed velocity evolution of SN 2023ixf was consistent with a linear growth pattern, confirming that the stellar wind of this SN was accelerated by radiation. Consequently, the upper limit stellar wind velocity of SN 2023ixf before acceleration was 55 km s^{-1} , slightly higher than that of SN 2024ggi. This variety in wind velocity shows that we need a larger sample to explore the range of the RSG wind.

In the early high-resolution spectra of SN 2024ggi and SN 2023ixf, a blueshift in all of the emission lines is seen after correcting for the rotational velocity of the host based on Na I D absorption lines. However, the amount of blueshift between lines for these SNe is different. For SN 2024ggi, we found all the major lines to be shifted by -75 km s^{-1} in the first two epochs, whereas, in the case of SN 2023ixf, different lines were shifted by differ-

ent velocities ranging from 0 to -150 or -200 km s^{-1} (Smith et al. 2023). This blueshift in narrow emission lines has been seen before in the early spectra of interacting SNe, implying that they are emitted by CSM expanding towards the observer relative to the SN (Groh 2014; Shivvers et al. 2015; Gräfener & Vink 2016; Smith et al. 2023). It is difficult to compare the velocity evolution of SN 2024ggi to SN 2023ixf, as we have only two high-resolution spectra of SN 2024ggi where flash narrow emission lines are present. However, for the first two epochs, we find that the strength of the lines in both SNe evolves in a similar fashion. We find the FWHM of all the lines to decline in the second epoch except for C IV, which is also seen in SN 2023ixf (Figure 4 in Smith et al. 2023).

Finally, for both SNe, no precursor activity is observed, as shown in Figure 5. The nondetection limit for SN 2023ixf is deeper (Dong et al. 2023; Ransome et al. 2024) compared to SN 2024ggi. In both cases, precursor activity is not seen during the mass-loss period calculated from R_{CSM} and v_w .

7. CONCLUSIONS

We have presented high-cadence, multi-wavelength photometric and spectroscopic follow-up of the nearby Type II SN 2024ggi in NGC3621. In this paper, we focus on the early evolution. The major results from our analysis include:

1. We have obtained an unprecedented, high-cadence multi-wavelength photometric data set beginning only a few hours after explosion, providing a great opportunity to study the very early light-curve evolution. We also utilized ATLAS forced photometry at the location of SN 2024ggi to search for precursor activity and found no precursor emission down to ~ -9 mag, as shown in Figure 5.
2. We find the first 24 hours of data could not be matched by current shock-cooling models (Figure 9). This could be due to CSM interaction associated with extended shock breakout.
3. The $B - V$ color evolution during this phase shows a unique blueward evolution over the first two days (Figure 8). This behavior has been seen previously for very few SNe, and never with the time resolution achieved for SN 2024ggi.
4. In the early spectra of SN 2024ggi, we clearly identify high-ionization lines. The line strengths evolve quickly (over a several-hour time scale), and they vanish by +3.6 days after the explosion. From this, we calculate the CSM radius to be $\sim 2.3 \times 10^{14} \text{ cm}$.

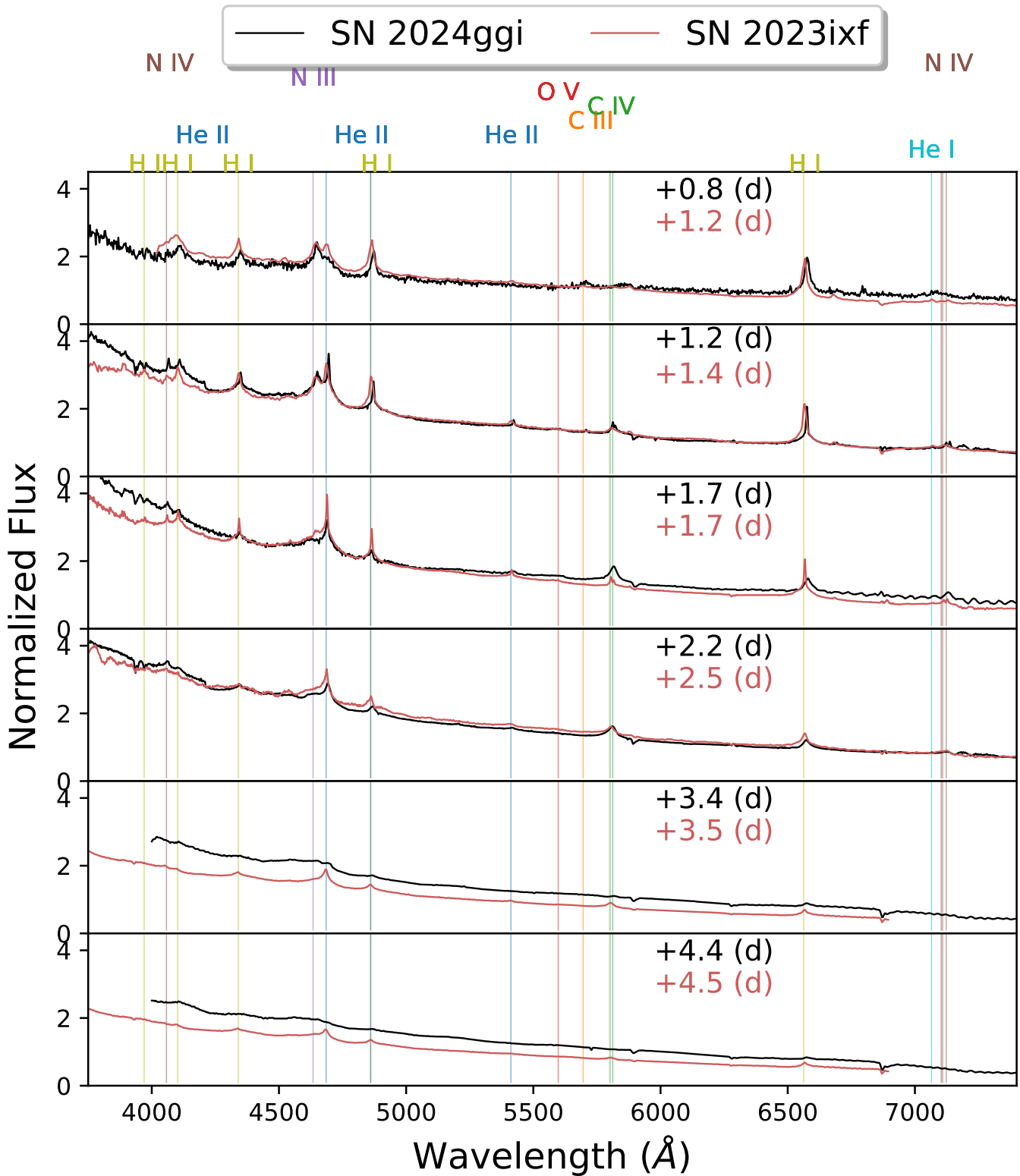


Figure 15. Optical spectral comparison of SN 2024ggi (black) and SN 2023ixf (red) for the first ~ 4.5 days after explosion. Interesting lines are identified and the epoch for each panel is shown for the two SNe. The first epoch of SN 2023ixf is several hours later than SN 2024ggi, where the He II line is still developing. Most of the lines are present for both the SNe. However, the strength of the lines rapidly declines for SN 2024ggi, with almost all the flash features vanishing by day 3.5, whereas the SN 2023ixf lines decline more slowly and are present even at +5.3 days. This difference can point to the CSM around SN 2024ggi being more confined than the CSM around SN 2023ixf.

5. Comparison of the early spectra with theoretical models by [Boian & Groh \(2019\)](#) and [Dessart et al. \(2017b\)](#) constrain the mass-loss rate for the progenitor star to be $10^{-2} - 10^{-3} M_{\odot} \text{ yr}^{-1}$.
6. From high-resolution data we constrain the RSG progenitor wind velocity to be $37 \pm 4 \text{ km s}^{-1}$.

SN 2024ggi has been extensively followed in various wavelengths ranging from γ -rays to X-rays to radio. There was no detection in γ -rays, but various groups detected X-ray photons at +2.3, +2.6, and +3.1 days after the explosion ([Zhang et al. 2024b](#); [Margutti & Grefenstette 2024](#); [Lutovinov et al. 2024](#)). Incidentally, these epochs coincide with the detection of flash features in the optical spectra. In addition, around 3 weeks after the explosion, there was a radio detection at the location of SN 2024ggi ([Ryder et al. 2024](#)). X-ray and radio detections along with flash features in early spectra all point to the presence of CSM interaction for SN 2024ggi.

The discovery of two core-collapse SNe in the very nearby universe within the last year (SN 2024ggi and SN 2023ixf) provides us with a great opportunity to compare and contrast their properties with high-quality data for years to come. These studies will offer us an unprecedented opportunity to understand the progenitor system, their environment, and the explosion mechanism in greater detail. Future observations of SN 2024ggi will add to our understanding of this supernova and could explain the unique early photometric color evolution to the rise of the light-curve, as well as the spectroscopic behavior.

ACKNOWLEDGMENTS

We would like to thank the anonymous referee for their thorough and constructive comments which has helped to improve the paper.

Based on observations obtained at the international Gemini Observatory (GS-2024A-Q-123, PI: Pearson), a program of NSF’s NOIRLab, which is managed by the Association of Universities for Research in Astronomy (AURA) under a cooperative agreement with the National Science Foundation. On behalf of the Gemini Observatory partnership: the National Science Foundation (United States), National Research Council (Canada), Agencia Nacional de Investigación y Desarrollo (Chile), Ministerio de Ciencia, Tecnología e Innovación (Argentina), Ministério da Ciência, Tecnologia, Inovações e Comunicações (Brazil), and Korea Astronomy and Space Science Institute (Republic of Korea).

The SALT spectra presented here were obtained through the Rutgers University SALT programs 2023-1-MLT-008, 2023-2-SCI-030, and 2024-1-MLT-003 (PI: Jha).

Time-domain research by the University of Arizona team and D.J.S. is supported by NSF grants AST-1821987, 1813466, 1908972, 2108032, and 2308181, and by the Heising-Simons Foundation under grant #2020-1864. The research by Y.D., S.V., N.M., and E.H. is supported by NSF grant AST-2008108.

This work makes use of data from the Las Cumbres Observatory global telescope network. The LCO team is supported by NSF grants AST-1911225 and AST-1911151.

Research by Y.D., S.V., N.M.R., and E.H. is supported by NSF grant AST-2008108. K.A.B. is supported by an LSSTC Catalyst Fellowship; this publication was thus made possible through the support of Grant 62192 from the John Templeton Foundation to LSSTC. The opinions expressed in this publication are those of the authors and do not necessarily reflect the views of LSSTC or the John Templeton Foundation. This work makes use of data taken with the Las Cumbres Observatory global telescope network. C.P.G. acknowledges financial support from the Secretary of Universities and Research (Government of Catalonia) and by the Horizon 2020 Research and Innovation Programme of the European Union under the Marie Skłodowska-Curie and the Beatriu de Pinós 2021 BP 00168 programme, from the Spanish Ministerio de Ciencia e Innovación (MCIN) and the Agencia Estatal de Investigación (AEI) 10.13039/501100011033 under the PID2020-115253GA-I00 HOSTFLOWS project, and the program Unidad de Excelencia María de Maeztu CEX2020-001058-M.

This paper includes data gathered with the 6.5m Magellan Telescopes located at Las Campanas Observatory, Chile.

This research has made use of the NASA Astrophysics Data System (ADS) Bibliographic Services, and the NASA/IPAC Infrared Science Archive (IRSA), which is funded by the National Aeronautics and Space Administration and operated by the California Institute of Technology. This work made use of data supplied by the UK Swift Science Data Centre at the University of Leicester. GEM acknowledges support from the University of Toronto Arts & Science Post-doctoral Fellowship program, the Dunlap Institute, and the Natural Sciences and Engineering Research Council of Canada (NSERC) through grant RGPIN-2022-04794. We acknowledge the support of the staff of the LJT. Funding for the LJT has been provided by the CAS and the People’s Government of Yunnan Province. J.Z. is supported by the National Key R&D Program of China with No. 2021YFA1600404, the National Natural Science Foundation of China (12173082), the Yunnan Province Foundation (202201AT070069), and the Inter-

national Centre of Supernovae, Yunnan Key Laboratory (No. 202302AN360001). R.R.M. gratefully acknowledges support by the ANID BASAL project FB210003.

Facilities: Las Cumbres Observatory, SALT (RSS & HRS), Gemini:South (GMOS), Swift (UVOT), Magellan:Clay (MIKE), Bok (B&C)

Software: Astropy (Astropy Collaboration et al. 2013; Price-Whelan et al. 2018; Astropy Collaboration

et al. 2022), Photutils (Bradley et al. 2019), Panacea, BANZAI (McCully et al. 2018), Light Curve Fitting (Hosseinzadeh & Gomez 2020), Matplotlib (Hunter 2007), Numpy (Harris et al. 2020), Scipy (Virtanen et al. 2020), IRAF (Tody 1986, 1993), PySALT (Crawford et al. 2010b), `lcogtsnpipe` (Valenti et al. 2016)

REFERENCES

- Andrews, J. E., Pearson, J., Hosseinzadeh, G., et al. 2024, *ApJ*, 965, 85, doi: [10.3847/1538-4357/ad2a49](https://doi.org/10.3847/1538-4357/ad2a49)
- Arcavi, I. 2022, *ApJ*, 937, 75, doi: [10.3847/1538-4357/ac90c0](https://doi.org/10.3847/1538-4357/ac90c0)
- Astropy Collaboration, Robitaille, T. P., Tollerud, E. J., et al. 2013, *A&A*, 558, A33, doi: [10.1051/0004-6361/201322068](https://doi.org/10.1051/0004-6361/201322068)
- Astropy Collaboration, Price-Whelan, A. M., Lim, P. L., et al. 2022, *ApJ*, 935, 167, doi: [10.3847/1538-4357/ac7c74](https://doi.org/10.3847/1538-4357/ac7c74)
- Beasor, E. R., Davies, B., Smith, N., et al. 2020, *MNRAS*, 492, 5994, doi: [10.1093/mnras/staa255](https://doi.org/10.1093/mnras/staa255)
- Bernstein, R., Shtetman, S. A., Gunnels, S. M., Mochnacki, S., & Athey, A. E. 2003, in *Society of Photo-Optical Instrumentation Engineers (SPIE) Conference Series*, Vol. 4841, Instrument Design and Performance for Optical/Infrared Ground-based Telescopes, ed. M. Iye & A. F. M. Moorwood, 1694–1704, doi: [10.1117/12.461502](https://doi.org/10.1117/12.461502)
- Boian, I., & Groh, J. H. 2019, *A&A*, 621, A109, doi: [10.1051/0004-6361/201833779](https://doi.org/10.1051/0004-6361/201833779)
- Bostroem, K. A., Pearson, J., Shrestha, M., et al. 2023, arXiv e-prints, arXiv:2306.10119, doi: [10.48550/arXiv.2306.10119](https://doi.org/10.48550/arXiv.2306.10119)
- Bradley, L., Sipőcz, B., Robitaille, T., et al. 2019, *astropy/photutils: v0.6*, doi: [10.5281/zenodo.2533376](https://doi.org/10.5281/zenodo.2533376)
- Bradley, L., Sipőcz, B., Robitaille, T., et al. 2022, *astropy/photutils: 1.6.0, 1.6.0*, Zenodo, Zenodo, doi: [10.5281/zenodo.7419741](https://doi.org/10.5281/zenodo.7419741)
- Breeveld, A. A., Curran, P. A., Hoversten, E. A., et al. 2010, *MNRAS*, 406, 1687, doi: [10.1111/j.1365-2966.2010.16832.x](https://doi.org/10.1111/j.1365-2966.2010.16832.x)
- Brown, T. M., Baliber, N., Bianco, F. B., et al. 2013, *PASP*, 125, 1031, doi: [10.1086/673168](https://doi.org/10.1086/673168)
- Bruch, R. J., Gal-Yam, A., Schulze, S., et al. 2021, *ApJ*, 912, 46, doi: [10.3847/1538-4357/abef05](https://doi.org/10.3847/1538-4357/abef05)
- Bruch, R. J., Gal-Yam, A., Yaron, O., et al. 2023, *ApJ*, 952, 119, doi: [10.3847/1538-4357/acd8be](https://doi.org/10.3847/1538-4357/acd8be)
- Chen, X., Kumar, B., Er, X., et al. 2024, arXiv e-prints, arXiv:2405.07964, doi: [10.48550/arXiv.2405.07964](https://doi.org/10.48550/arXiv.2405.07964)
- Chugai, N. N., Blinnikov, S. I., Cumming, R. J., et al. 2004, *MNRAS*, 352, 1213, doi: [10.1111/j.1365-2966.2004.08011.x](https://doi.org/10.1111/j.1365-2966.2004.08011.x)
- Crause, L. A., Sharples, R. M., Bramall, D. G., et al. 2014, in *Society of Photo-Optical Instrumentation Engineers (SPIE) Conference Series*, Vol. 9147, Ground-based and Airborne Instrumentation for Astronomy V, ed. S. K. Ramsay, I. S. McLean, & H. Takami, 91476T, doi: [10.1117/12.2055635](https://doi.org/10.1117/12.2055635)
- Crawford, S. M., Still, M., Schellart, P., et al. 2010a, in *Society of Photo-Optical Instrumentation Engineers (SPIE) Conference Series*, Vol. 7737, Observatory Operations: Strategies, Processes, and Systems III, ed. D. R. Silva, A. B. Peck, & B. T. Soifer, 773725, doi: [10.1117/12.857000](https://doi.org/10.1117/12.857000)
- Crawford, S. M., Still, M., Schellart, P., et al. 2010b, in *Society of Photo-Optical Instrumentation Engineers (SPIE) Conference Series*, Society of Photo-Optical Instrumentation Engineers (SPIE) Conference Series, 25, doi: [10.1117/12.857000](https://doi.org/10.1117/12.857000)
- de Jager, C., Nieuwenhuijzen, H., & van der Hucht, K. A. 1988, *A&AS*, 72, 259
- Dessart, L., Hillier, D. J., & Audit, E. 2017a, *A&A*, 605, A83, doi: [10.1051/0004-6361/201730942](https://doi.org/10.1051/0004-6361/201730942)
- . 2017b, *A&A*, 605, A83, doi: [10.1051/0004-6361/201730942](https://doi.org/10.1051/0004-6361/201730942)
- Dessart, L., Hillier, D. J., Waldman, R., & Livne, E. 2013, *MNRAS*, 433, 1745, doi: [10.1093/mnras/stt861](https://doi.org/10.1093/mnras/stt861)
- Deutsch, A. J. 1956, *ApJ*, 123, 210, doi: [10.1086/146152](https://doi.org/10.1086/146152)
- Dong, Y., Sand, D. J., Valenti, S., et al. 2023, *ApJ*, 957, 28, doi: [10.3847/1538-4357/acef18](https://doi.org/10.3847/1538-4357/acef18)
- Ekström, S., Georgy, C., Eggenberger, P., et al. 2012, *A&A*, 537, A146, doi: [10.1051/0004-6361/201117751](https://doi.org/10.1051/0004-6361/201117751)
- Förster, F., Moriya, T. J., Maureira, J. C., et al. 2018, *Nature Astronomy*, 2, 808, doi: [10.1038/s41550-018-0563-4](https://doi.org/10.1038/s41550-018-0563-4)

- Gal-Yam, A., Arcavi, I., Ofek, E. O., et al. 2014, *Nature*, 509, 471, doi: [10.1038/nature13304](https://doi.org/10.1038/nature13304)
- Gehrels, N., Chincarini, G., Giommi, P., et al. 2004, *ApJ*, 611, 1005, doi: [10.1086/422091](https://doi.org/10.1086/422091)
- Gimeno, G., Roth, K., Chiboucas, K., et al. 2016, in *Society of Photo-Optical Instrumentation Engineers (SPIE) Conference Series*, Vol. 9908, Proc. SPIE, 99082S, doi: [10.1117/12.2233883](https://doi.org/10.1117/12.2233883)
- Goldberg, J. A., Jiang, Y.-F., & Bildsten, L. 2022, *ApJ*, 933, 164, doi: [10.3847/1538-4357/ac75e3](https://doi.org/10.3847/1538-4357/ac75e3)
- Gräfener, G., & Vink, J. S. 2016, *MNRAS*, 455, 112, doi: [10.1093/mnras/stv2283](https://doi.org/10.1093/mnras/stv2283)
- Groh, J. H. 2014, *A&A*, 572, L11, doi: [10.1051/0004-6361/201424852](https://doi.org/10.1051/0004-6361/201424852)
- Harris, C. R., Millman, K. J., van der Walt, S. J., et al. 2020, *Nature*, 585, 357, doi: [10.1038/s41586-020-2649-2](https://doi.org/10.1038/s41586-020-2649-2)
- Haynie, A., & Piro, A. L. 2021, *ApJ*, 910, 128, doi: [10.3847/1538-4357/abe938](https://doi.org/10.3847/1538-4357/abe938)
- Henden, A. A., Welch, D. L., Terrell, D., & Levine, S. E. 2009, in *American Astronomical Society Meeting Abstracts*, Vol. 214, American Astronomical Society Meeting Abstracts #214, 407.02
- Hillier, D. J., & Dessart, L. 2012, *MNRAS*, 424, 252, doi: [10.1111/j.1365-2966.2012.21192.x](https://doi.org/10.1111/j.1365-2966.2012.21192.x)
- . 2019, *A&A*, 631, A8, doi: [10.1051/0004-6361/201935100](https://doi.org/10.1051/0004-6361/201935100)
- Hillier, D. J., & Miller, D. L. 1998, *ApJ*, 496, 407, doi: [10.1086/305350](https://doi.org/10.1086/305350)
- Hiramatsu, D., Howell, D. A., Van Dyk, S. D., et al. 2021, *Nature Astronomy*, 5, 903, doi: [10.1038/s41550-021-01384-2](https://doi.org/10.1038/s41550-021-01384-2)
- Hiramatsu, D., Tsuna, D., Berger, E., et al. 2023a, *ApJL*, 955, L8, doi: [10.3847/2041-8213/acf299](https://doi.org/10.3847/2041-8213/acf299)
- . 2023b, *ApJL*, 955, L8, doi: [10.3847/2041-8213/acf299](https://doi.org/10.3847/2041-8213/acf299)
- Hook, I. M., Jørgensen, I., Allington-Smith, J. R., et al. 2004, *PASP*, 116, 425, doi: [10.1086/383624](https://doi.org/10.1086/383624)
- Hosseinzadeh, G., Bostroem, K. A., & Gomez, S. 2023, *Light Curve Fitting v0.9.0*, Zenodo, doi: [10.5281/zenodo.8049154](https://doi.org/10.5281/zenodo.8049154)
- Hosseinzadeh, G., & Gomez, S. 2020, *Light Curve Fitting, v0.2.0*, Zenodo, Zenodo, doi: [10.5281/zenodo.4312178](https://doi.org/10.5281/zenodo.4312178)
- Hosseinzadeh, G., Valenti, S., McCully, C., et al. 2018, *ApJ*, 861, 63, doi: [10.3847/1538-4357/aac5f6](https://doi.org/10.3847/1538-4357/aac5f6)
- Hosseinzadeh, G., Farah, J., Shrestha, M., et al. 2023, arXiv e-prints, arXiv:2306.06097, doi: [10.48550/arXiv.2306.06097](https://doi.org/10.48550/arXiv.2306.06097)
- Hunter, J. D. 2007, *Computing in Science and Engineering*, 9, 90, doi: [10.1109/MCSE.2007.55](https://doi.org/10.1109/MCSE.2007.55)
- Irani, I., Morag, J., Gal-Yam, A., et al. 2023, arXiv e-prints, arXiv:2310.16885, doi: [10.48550/arXiv.2310.16885](https://doi.org/10.48550/arXiv.2310.16885)
- Itagaki, K. 2023, *TNSTR*, 1158, 1
- Jacobson-Galán, W. V., Dessart, L., Jones, D. O., et al. 2022, *ApJ*, 924, 15, doi: [10.3847/1538-4357/ac3f3a](https://doi.org/10.3847/1538-4357/ac3f3a)
- Jacobson-Galán, W. V., Dessart, L., Margutti, R., et al. 2023, *ApJL*, 954, L42, doi: [10.3847/2041-8213/acf2ec](https://doi.org/10.3847/2041-8213/acf2ec)
- Jacobson-Galán, W. V., Dessart, L., Davis, K. W., et al. 2024a, arXiv e-prints, arXiv:2403.02382, doi: [10.48550/arXiv.2403.02382](https://doi.org/10.48550/arXiv.2403.02382)
- Jacobson-Galán, W. V., Davis, K. W., Kilpatrick, C. D., et al. 2024b, arXiv e-prints, arXiv:2404.19006, doi: [10.48550/arXiv.2404.19006](https://doi.org/10.48550/arXiv.2404.19006)
- Jacobson-Galán, W. V., Dessart, L., Davis, K. W., et al. 2024c, arXiv e-prints, arXiv:2403.02382, doi: [10.48550/arXiv.2403.02382](https://doi.org/10.48550/arXiv.2403.02382)
- Johnson, S. A., Kochanek, C. S., & Adams, S. M. 2018, *MNRAS*, 480, 1696, doi: [10.1093/mnras/sty1966](https://doi.org/10.1093/mnras/sty1966)
- Jura, M., & Kleinmann, S. G. 1990, *ApJS*, 73, 769, doi: [10.1086/191488](https://doi.org/10.1086/191488)
- Katz, B., Sapir, N., & Waxman, E. 2012, *ApJ*, 747, 147, doi: [10.1088/0004-637X/747/2/147](https://doi.org/10.1088/0004-637X/747/2/147)
- Kelson, D. D. 2003, *PASP*, 115, 688, doi: [10.1086/375502](https://doi.org/10.1086/375502)
- Kelson, D. D., Illingworth, G. D., van Dokkum, P. G., & Franx, M. 2000, *ApJ*, 531, 159, doi: [10.1086/308445](https://doi.org/10.1086/308445)
- Khazov, D., Yaron, O., Gal-Yam, A., et al. 2016, *ApJ*, 818, 3, doi: [10.3847/0004-637X/818/1/3](https://doi.org/10.3847/0004-637X/818/1/3)
- Killestein, T., Ackley, K., Kotak, R., et al. 2024a, *Transient Name Server AstroNote*, 101, 1
- . 2024b, *Transient Name Server AstroNote*, 101, 1
- Kniazev, A. Y., Gvaramadze, V. V., & Berdnikov, L. N. 2016, *MNRAS*, 459, 3068, doi: [10.1093/mnras/stw889](https://doi.org/10.1093/mnras/stw889)
- Kniazev, A. Y., Gvaramadze, V. V., & Berdnikov, L. N. 2017, in *Astronomical Society of the Pacific Conference Series*, Vol. 510, Stars: From Collapse to Collapse, ed. Y. Y. Balega, D. O. Kudryavtsev, I. I. Romanyuk, & I. A. Yakunin, 480, doi: [10.48550/arXiv.1612.00292](https://doi.org/10.48550/arXiv.1612.00292)
- Labrie, K., Anderson, K., Cárdenes, R., Simpson, C., & Turner, J. E. H. 2019, in *Astronomical Society of the Pacific Conference Series*, Vol. 523, *Astronomical Data Analysis Software and Systems XXVII*, ed. P. J. Teuben, M. W. Pound, B. A. Thomas, & E. M. Warner, 321
- Li, G., Hu, M., Li, W., et al. 2024, *Nature*, 627, 754, doi: [10.1038/s41586-023-06843-6](https://doi.org/10.1038/s41586-023-06843-6)
- Lutovinov, A. A., Semena, A. N., Mereminskiy, I. A., et al. 2024, *The Astronomer's Telegram*, 16586, 1
- Margutti, R., & Grefenstette, B. 2024, *The Astronomer's Telegram*, 16587, 1
- Masci, F. 2011, *Computing flux upper-limits for non-detections*. <https://web.ipac.caltech.edu/staff/fmasci/home/mystats/UpperLimits.FM2011.pdf>

- McCully, C., Volgenau, N. H., Harbeck, D.-R., et al. 2018, in Society of Photo-Optical Instrumentation Engineers (SPIE) Conference Series, Vol. 10707, Software and Cyberinfrastructure for Astronomy V, ed. J. C. Guzman & J. Ibsen, 107070K, doi: [10.1117/12.2314340](https://doi.org/10.1117/12.2314340)
- Meza Retamal, N., Dong, Y., Bostroem, K. A., et al. 2024, arXiv e-prints, arXiv:2401.04027, doi: [10.48550/arXiv.2401.04027](https://doi.org/10.48550/arXiv.2401.04027)
- Morag, J., Irani, I., Sapir, N., & Waxman, E. 2024, MNRAS, 528, 7137, doi: [10.1093/mnras/stae374](https://doi.org/10.1093/mnras/stae374)
- Morag, J., Sapir, N., & Waxman, E. 2023, MNRAS, 522, 2764, doi: [10.1093/mnras/stad899](https://doi.org/10.1093/mnras/stad899)
- Morozova, V., Piro, A. L., & Valenti, S. 2018, ApJ, 858, 15, doi: [10.3847/1538-4357/aab9a6](https://doi.org/10.3847/1538-4357/aab9a6)
- Munari, U., & Zwitter, T. 1997, A&A, 318, 269
- Neustadt, J. M. M., Kochanek, C. S., & Smith, M. R. 2024, MNRAS, 527, 5366, doi: [10.1093/mnras/stad3073](https://doi.org/10.1093/mnras/stad3073)
- Ofek, E. O., Rabinak, I., Neill, J. D., et al. 2010, ApJ, 724, 1396, doi: [10.1088/0004-637X/724/2/1396](https://doi.org/10.1088/0004-637X/724/2/1396)
- Ofek, E. O., Sullivan, M., Shaviv, N. J., et al. 2014, ApJ, 789, 104, doi: [10.1088/0004-637X/789/2/104](https://doi.org/10.1088/0004-637X/789/2/104)
- Pessi, T., Cartier, R., Hueichapan, E., et al. 2024, arXiv e-prints, arXiv:2405.02274, doi: [10.48550/arXiv.2405.02274](https://doi.org/10.48550/arXiv.2405.02274)
- Poznanski, D., Prochaska, J. X., & Bloom, J. S. 2012, MNRAS, 426, 1465, doi: [10.1111/j.1365-2966.2012.21796.x](https://doi.org/10.1111/j.1365-2966.2012.21796.x)
- Price-Whelan, A. M., Sipócz, B. M., Günther, H. M., et al. 2018, AJ, 156, 123, doi: [10.3847/1538-3881/aabc4f](https://doi.org/10.3847/1538-3881/aabc4f)
- Rabinak, I., & Waxman, E. 2011, ApJ, 728, 63, doi: [10.1088/0004-637X/728/1/63](https://doi.org/10.1088/0004-637X/728/1/63)
- Ransome, C. L., Villar, V. A., Tartaglia, A., et al. 2024, ApJ, 965, 93, doi: [10.3847/1538-4357/ad2df7](https://doi.org/10.3847/1538-4357/ad2df7)
- Reichart, D., Nysewander, M., Moran, J., et al. 2005, II Nuovo Cimento C, vol. 28, Issue 4, p.767, 28, 767, doi: [10.1393/ncc/i2005-10149-6](https://doi.org/10.1393/ncc/i2005-10149-6)
- Rest, S., Rest, A., Kilpatrick, C. D., et al. 2024, arXiv e-prints, arXiv:2405.03747, doi: [10.48550/arXiv.2405.03747](https://doi.org/10.48550/arXiv.2405.03747)
- Richmond, M. W., Treffers, R. R., Filippenko, A. V., et al. 1994, AJ, 107, 1022, doi: [10.1086/116915](https://doi.org/10.1086/116915)
- Roming, P. W. A., Kennedy, T. E., Mason, K. O., et al. 2005, SSRv, 120, 95, doi: [10.1007/s11214-005-5095-4](https://doi.org/10.1007/s11214-005-5095-4)
- Ryder, S., Maeda, K., Chandra, P., Alsaberi, R., & Kotak, R. 2024, The Astronomer's Telegram, 16616, 1
- Saha, A., Thim, F., Tammann, G. A., Reindl, B., & Sandage, A. 2006, ApJS, 165, 108, doi: [10.1086/503800](https://doi.org/10.1086/503800)
- Sapir, N., Katz, B., & Waxman, E. 2011, ApJ, 742, 36, doi: [10.1088/0004-637X/742/1/36](https://doi.org/10.1088/0004-637X/742/1/36)
- . 2013, ApJ, 774, 79, doi: [10.1088/0004-637X/774/1/79](https://doi.org/10.1088/0004-637X/774/1/79)
- Sapir, N., & Waxman, E. 2017, ApJ, 838, 130, doi: [10.3847/1538-4357/aa64df](https://doi.org/10.3847/1538-4357/aa64df)
- Schlafly, E. F., & Finkbeiner, D. P. 2011, ApJ, 737, 103, doi: [10.1088/0004-637X/737/2/103](https://doi.org/10.1088/0004-637X/737/2/103)
- Shingles, L., Smith, K. W., Young, D. R., et al. 2021, Transient Name Server AstroNote, 7, 1
- Shivvers, I., Groh, J. H., Mauerhan, J. C., et al. 2015, ApJ, 806, 213, doi: [10.1088/0004-637X/806/2/213](https://doi.org/10.1088/0004-637X/806/2/213)
- Shrestha, M., Pearson, J., Wyatt, S., et al. 2024, ApJ, 961, 247, doi: [10.3847/1538-4357/ad11e1](https://doi.org/10.3847/1538-4357/ad11e1)
- Smartt, S. J. 2009, ARA&A, 47, 63, doi: [10.1146/annurev-astro-082708-10173710.48550/arXiv.0908.0700](https://doi.org/10.1146/annurev-astro-082708-10173710.48550/arXiv.0908.0700)
- . 2015, PASA, 32, e016, doi: [10.1017/pasa.2015.17](https://doi.org/10.1017/pasa.2015.17)
- Smith, K. W., Smartt, S. J., Young, D. R., et al. 2020, PASP, 132, 085002, doi: [10.1088/1538-3873/ab936e](https://doi.org/10.1088/1538-3873/ab936e)
- Smith, M. P., Nordsieck, K. H., Burgh, E. B., et al. 2006, in Society of Photo-Optical Instrumentation Engineers (SPIE) Conference Series, Vol. 6269, Society of Photo-Optical Instrumentation Engineers (SPIE) Conference Series, ed. I. S. McLean & M. Iye, 62692A, doi: [10.1117/12.672415](https://doi.org/10.1117/12.672415)
- Smith, N., & McCray, R. 2007, ApJL, 671, L17, doi: [10.1086/524681](https://doi.org/10.1086/524681)
- Smith, N., Pearson, J., Sand, D. J., et al. 2023, ApJ, 956, 46, doi: [10.3847/1538-4357/acf366](https://doi.org/10.3847/1538-4357/acf366)
- Smith, N., Mauerhan, J. C., Cenko, S. B., et al. 2015, MNRAS, 449, 1876, doi: [10.1093/mnras/stv354](https://doi.org/10.1093/mnras/stv354)
- Soker, N. 2024, arXiv e-prints, arXiv:2406.17751, doi: [10.48550/arXiv.2406.17751](https://doi.org/10.48550/arXiv.2406.17751)
- Srivastav, S., Chen, T. W., Smartt, S. J., et al. 2024, Transient Name Server AstroNote, 100, 1
- Steehls, D., Galloway, D. K., Ackley, K., et al. 2022, MNRAS, 511, 2405, doi: [10.1093/mnras/stac013](https://doi.org/10.1093/mnras/stac013)
- Strotjohann, N. L., Ofek, E. O., Gal-Yam, A., et al. 2021, ApJ, 907, 99, doi: [10.3847/1538-4357/abd032](https://doi.org/10.3847/1538-4357/abd032)
- Tartaglia, L., Sand, D. J., Valenti, S., et al. 2018, ApJ, 853, 62, doi: [10.3847/1538-4357/aaa014](https://doi.org/10.3847/1538-4357/aaa014)
- Tartaglia, L., Sand, D. J., Groh, J. H., et al. 2021, ApJ, 907, 52, doi: [10.3847/1538-4357/abca8a](https://doi.org/10.3847/1538-4357/abca8a)
- Teja, R. S., Singh, A., Basu, J., et al. 2023, ApJL, 954, L12, doi: [10.3847/2041-8213/acef20](https://doi.org/10.3847/2041-8213/acef20)
- Terreran, G., Jacobson-Galán, W. V., Groh, J. H., et al. 2022, ApJ, 926, 20, doi: [10.3847/1538-4357/ac3820](https://doi.org/10.3847/1538-4357/ac3820)
- Tody, D. 1986, in Society of Photo-Optical Instrumentation Engineers (SPIE) Conference Series, Vol. 627, Instrumentation in astronomy VI, ed. D. L. Crawford, 733, doi: [10.1117/12.968154](https://doi.org/10.1117/12.968154)

- Tody, D. 1993, in *Astronomical Society of the Pacific Conference Series*, Vol. 52, *Astronomical Data Analysis Software and Systems II*, ed. R. J. Hanisch, R. J. V. Brissenden, & J. Barnes, 173
- Tonry, J., Denneau, L., Weiland, H., et al. 2024, *Transient Name Server Discovery Report*, 2024-1020, 1
- Tonry, J. L. 2011, *PASP*, 123, 58, doi: [10.1086/657997](https://doi.org/10.1086/657997)
- Tonry, J. L., Denneau, L., Heinze, A. N., et al. 2018, *PASP*, 130, 064505, doi: [10.1088/1538-3873/aabadf](https://doi.org/10.1088/1538-3873/aabadf)
- Valenti, S., Sand, D., Pastorello, A., et al. 2014, *MNRAS*, 438, 101, doi: [10.1093/mnras/slt171](https://doi.org/10.1093/mnras/slt171)
- Valenti, S., Howell, D. A., Stritzinger, M. D., et al. 2016, *MNRAS*, 459, 3939, doi: [10.1093/mnras/stw870](https://doi.org/10.1093/mnras/stw870)
- Virtanen, P., Gommers, R., Oliphant, T. E., et al. 2020, *Nature Methods*, 17, 261, doi: [10.1038/s41592-019-0686-2](https://doi.org/10.1038/s41592-019-0686-2)
- Wang, C.-J., Bai, J.-M., Fan, Y.-F., et al. 2019, *Research in Astronomy and Astrophysics*, 19, 149, doi: [10.1088/1674-4527/19/10/149](https://doi.org/10.1088/1674-4527/19/10/149)
- Waxman, E., & Katz, B. 2017, in *Handbook of Supernovae*, ed. A. W. Alsabti & P. Murdin (Springer), 967, doi: [10.1007/978-3-319-21846-5_33](https://doi.org/10.1007/978-3-319-21846-5_33)
- Xiang, D., Mo, J., Wang, X., et al. 2024, *ApJL*, 969, L15, doi: [10.3847/2041-8213/ad54b3](https://doi.org/10.3847/2041-8213/ad54b3)
- Yaron, O., Perley, D. A., Gal-Yam, A., et al. 2017, *Nature Physics*, 13, 510, doi: [10.1038/nphys4025](https://doi.org/10.1038/nphys4025)
- Young, D. 2022, *Plot Results from ATLAS Force Photometry Service*. <https://gist.github.com/thespacedoctor/86777fa5a9567b7939e8d84fd8cf6a76>
- Zhai, Q., Li, L., Zhang, J., & Wang, X. 2024a, *Transient Name Server Classification Report*, 2024-1031, 1
- . 2024b, *Transient Name Server Classification Report*, 2024-1031, 1
- Zhang, J., Wang, X., József, V., et al. 2020, *MNRAS*, 498, 84, doi: [10.1093/mnras/staa2273](https://doi.org/10.1093/mnras/staa2273)
- Zhang, J., Lin, H., Wang, X., et al. 2023, *Science Bulletin*, 68, 2548, doi: [10.1016/j.scib.2023.09.015](https://doi.org/10.1016/j.scib.2023.09.015)
- Zhang, J., Dessart, L., Wang, X., et al. 2024a, *ApJL*, 970, L18, doi: [10.3847/2041-8213/ad5da4](https://doi.org/10.3847/2041-8213/ad5da4)
- Zhang, J., Li, C. K., Cheng, H. Q., et al. 2024b, *The Astronomer's Telegram*, 16588, 1
- Zimmerman, E. A., Irani, I., Chen, P., et al. 2024, *Nature*, 627, 759, doi: [10.1038/s41586-024-07116-6](https://doi.org/10.1038/s41586-024-07116-6)